Astronomy & Astrophysics

Planck intermediate results

XLI. A map of lensing-induced *B*-modes

Planck Collaboration: P. A. R. Ade[82], N. Aghanim[54], M. Ashdown[64,6], J. Aumont[54], C. Baccigalupi[81], A. J. Banday[91,10], R. B. Barreiro[59], N. Bartolo[30,60], S. Basak[81], E. Battaner[92,93], K. Benabed[55,90], A. Benoit-Lévy[24,55,90], J.-P. Bernard[91,10], M. Bersanelli[33,47], P. Bielewicz[76,10,81], J. J. Bock[61,12], A. Bonaldi[62], L. Bonavera[59], J. R. Bond[9], J. Borrill[14,86], F. R. Bouchet[55,84], F. Boulanger[54], C. Burigana[46,31,48], R. C. Butler[46], E. Calabrese[88], J.-F. Cardoso[69,1,55], A. Catalano[70,67], H. C. Chiang[26,7], P. R. Christensen[77,35], D. L. Clements[52], S. Colombi[55,90], L. P. L. Colombo[23,61], C. Combet[70], B. P. Crill[61,12], A. Curto[59,6,64], F. Cuttaia[46], L. Danese[81], R. J. Davis[62], P. de Bernardis[32], G. de Zotti[43,81], J. Delabrouille[1], C. Dickinson[62], J. M. Diego[59], O. Doré[61,12], A. Ducout[55,52], X. Dupac[37], F. Elsner[24,55,90], T. A. Enßlin[74], H. K. Eriksen[57], F. Finelli[46,48], O. Forni[91,10], M. Frailis[45], A. A. Fraisse[26], E. Franceschi[46], S. Galeotta[45], S. Galli[63], K. Ganga[1], T. Ghosh[54], M. Giard[91,10], Y. Giraud-Héraud[1], E. Gjerløw[57], J. González-Nuevo[19,59], K. M. Górski[61,94], A. Gruppuso[46], J. E. Gudmundsson[89,79,26], D. L. Harrison[56,64], C. Hernández-Monteagudo[13,74], D. Herranz[59], S. R. Hildebrandt[61,12], A. Hornstrup[16], W. Hovest[74], G. Hurier[54], A. H. Jaffe[52], W. C. Jones[26], E. Keihänen[25], R. Keskitalo[14], T. S. Kisner[72], J. Knoche[74], L. Knox[27], M. Kunz[17,54,3], H. Kurki-Suonio[25,42], G. Lagache[5,54], A. Lähteenmäki[2,42], J.-M. Lamarre[67], A. Lasenby[6,64], M. Lattanzi[31], R. Leonardi[8], F. Levrier[67], P. B. Lilje[57], M. Linden-Vørnle[16], M. López-Caniego[37,59], P. M. Lubin[28], J. F. Macías-Pérez[70], B. Maffei[62], G. Maggio[45], D. Maino[33,47], N. Mandolesi[46,31], A. Mangilli[54,66], M. Maris[45], P. G. Martin[9], E. Martínez-González[59], S. Masi[32], S. Matarrese[30,60,40], P. R. Meinhold[28], A. Melchiorri[32,49], A. Mennella[33,47], M. Migliaccio[56,64], S. Mitra[51,61], M.-A. Miville-Deschênes[54,9], A. Moneti[55], L. Montier[91,10], G. Morgante[46], D. Mortlock[52], A. Moss[83], D. Munshi[82], J. A. Murphy[75], P. Naselsky[78,36], F. Nati[26], P. Natoli[31,4,46], C. B. Netterfield[20], H. U. Nørgaard-Nielsen[16], D. Novikov[73], I. Novikov[77,73], L. Pagano[32,49], F. Pajot[54], D. Paoletti[46,48], F. Pasian[45], G. Patanchon[1], O. Perdereau[66], L. Perotto[70,⋆], V. Pettorino[41], F. Piacentini[32], M. Piat[1], E. Pierpaoli[23], E. Pointecouteau[91,10], G. Polenta[4,44], G. W. Pratt[68], J. P. Rachen[21,74], M. Reinecke[74], M. Remazeilles[62,54,1], C. Renault[70], A. Renzi[34,50], I. Ristorcelli[91,10], G. Rocha[61,12], C. Rosset[1], M. Rossetti[33,47], G. Roudier[1,67,61], J. A. Rubiño-Martín[58,18], B. Rusholme[53], M. Sandri[46], D. Santos[70], M. Savelainen[25,42], G. Savini[80], D. Scott[22], L. D. Spencer[82], V. Stolyarov[6,87,65], R. Stompor[1], R. Sudiwala[82], R. Sunyaev[74,85], D. Sutton[56,64], A.-S. Suur-Uski[25,42], J.-F. Sygnet[55], J. A. Tauber[38], L. Terenzi[39,46], L. Toffolatti[19,59,46], M. Tomasi[33,47], M. Tristram[66], M. Tucci[17], J. Tuovinen[11], L. Valenziano[46], J. Valiviita[25,42], B. Van Tent[71], P. Vielva[59], F. Villa[46], L. A. Wade[61], B. D. Wandelt[55,90,29], I. K. Wehus[61], D. Yvon[15], A. Zacchei[45], and A. Zonca[28]

(Affiliations can be found after the references)

ABSTRACT

The secondary cosmic microwave background (CMB) *B*-modes stem from the post-decoupling distortion of the polarization *E*-modes due to the gravitational lensing effect of large-scale structures. These lensing-induced *B*-modes constitute both a valuable probe of the dark matter distribution and an important contaminant for the extraction of the primary CMB *B*-modes from inflation. *Planck* provides accurate nearly all-sky measurements of both the polarization *E*-modes and the integrated mass distribution via the reconstruction of the CMB lensing potential. By combining these two data products, we have produced an all-sky template map of the lensing-induced *B*-modes using a real-space algorithm that minimizes the impact of sky masks. The cross-correlation of this template with an observed (primordial and secondary) *B*-mode map can be used to measure the lensing *B*-mode power spectrum at multipoles up to 2000. In particular, when cross-correlating with the *B*-mode contribution directly derived from the *Planck* polarization maps, we obtain lensing-induced *B*-mode power spectrum measurement at a significance level of 12σ, which agrees with the theoretical expectation derived from the *Planck* best-fit Λ cold dark matter model. This unique nearly all-sky secondary *B*-mode template, which includes the lensing-induced information from intermediate to small ($10 \lesssim \ell \lesssim 1000$) angular scales, is delivered as part of the *Planck* 2015 public data release. It will be particularly useful for experiments searching for primordial *B*-modes, such as BICEP2/Keck Array or LiteBIRD, since it will enable an estimate to be made of the lensing-induced contribution to the measured total CMB *B*-modes.

Key words. cosmology: observations – cosmic background radiation – polarization – gravitational lensing: weak

1. Introduction

Cosmic microwave background (CMB) polarization anisotropies can be decomposed into curl-free *E*-modes and gradient-free *B*-modes. In contrast to primordial *E*-modes, primordial *B*-modes are sourced only by tensor perturbations (Polnarev 1985; Spergel & Zaldarriaga 1997; Kamionkowski et al. 1997; Seljak & Zaldarriaga 1997) that can be formed in the pre-decoupling Universe due to an early inflationary phase (Grishchuk 1975; Starobinsky 1979, 1982). Thus, primordial *B*-modes of the CMB polarization are a direct probe of cosmological inflation (see Guth 1981; Linde 1982, for details on inflationary theory). The measurement of the primordial

B-mode power spectrum, which peaks at degree angular scales, is the main target of a plethora of ground-based experiments and satellite proposals. There was great excitement in early 2014 when *B*-modes at the relevant angular scales detected by the BICEP2 experiment were interpreted as evidence of inflationary gravitational waves (Ade et al. 2014a). Investigating the polarized dust emission in the BICEP2 observation field using the 353-GHz data, *Planck*[1] revealed a

---

[1] *Planck* (http://www.esa.int/Planck) is a project of the European Space Agency (ESA) with instruments provided by two scientific consortia funded by ESA member states and led by Principal Investigators from France and Italy, telescope reflectors provided through a collaboration between ESA and a scientific consortium led and funded by Denmark, and additional contributions from NASA (USA).

higher dust contamination level than expected from pre-*Planck* foreground models (Planck Collaboration Int. XXX 2016). In BICEP2/Keck Array and Planck Collaborations (2015), a joint analysis of the BICEP2/Keck Array data at 100 and 150 GHz and the full-mission *Planck* data (particularly the 353-GHz polarized data) has been conducted. This provides the state-of-the-art constraints on the tensor-to-scalar ratio, r, which is currently consistent with no detection of a primordial *B*-mode signal. When combined with the limit derived from the temperature data (as discussed in Planck Collaboration XVI 2014 and Planck Collaboration XIII 2016), the current 95% upper limit is $r < 0.08$, which already rules out some of the simplest inflationary potentials (Planck Collaboration XX 2016). We stand at the threshold of a particularly exciting epoch that is marked by several ongoing or near-future ground-based experimental efforts, based on technology that is sensitive and mature enough to probe the primordial *B*-modes to theoretically interesting levels.

In addition to the primordial contribution, a secondary contribution is expected from the post-decoupling distortion of the CMB polarization due to the effect of gravitational lensing (see Lewis & Challinor 2006, for a review of CMB lensing). In particular, the lensing of the primordial CMB polarization *E*-modes leads to an additional *B*-mode contribution. The secondary *B*-mode contribution to the C_ℓ^{BB} power spectrum dominates over the primary one at $\ell \gtrsim 150$, even for large values of the tensor-to-scalar ratio, ($r \sim 1$). Thus, it must be corrected for, in order to measure the imprint of primordial tensor modes. This correction is generally referred to as "delensing".

The secondary *B*-mode power spectrum can be estimated by cross-correlating the total observed *B*-mode map with a template constructed by combining a tracer of the gravitational potential and an estimate of the primordial *E*-modes. Using such a cross-correlation approach, the SPTpol team (Hanson et al. 2013) reported the first estimate of the lensing *B*-mode power spectrum, consisting of a roughly $\lesssim 8\sigma$ measurement in the multipole range $300 < \ell < 2750$ using *Herschel*-SPIRE data as the mass tracer. The POLARBEAR collaboration detected the lensing *B*-modes using CMB polarization data by fitting an amplitude relative to the theoretical expectations to their CMB polarization trispectrum measurements, and reported a 4.2σ rejection of the null-hypothesis (Ade et al. 2014b). Similarly, the ACTPol team reported 3.2σ evidence of the lensing *B*-mode signal within its first season data, using the correlation of the lensing potential estimate and the cosmic infrared background fluctuations measured by *Planck* (van Engelen et al. 2015). Finally, using the full mission temperature and polarization data, *Planck* obtained a template-based cross-correlation measurement of the lensing *B*-mode power spectrum that covers the multipole range $100 < \ell < 2000$, at a significance level of approximately 10σ, as described in Planck Collaboration XV (2016).

Secondary *B*-modes dominate any potential primordial *B*-modes at high multipoles, thus the high-ℓ *BB* power spectrum of the observed polarization maps can also be used to make a lensing-induced *B*-mode measurement. The POLARBEAR collaboration reported the first *BB* measurement (at around 2σ) of the *B*-mode power spectrum in the multipole range $500 < \ell < 2100$ (The Polarbear Collaboration 2014). The SPTpol experiment also made a *BB* estimate of the lensing *B*-modes in the range $300 < \ell < 2300$, representing a $>4\sigma$ detection Keisler et al. (2015). Moreover, a non-zero lensing *B*-mode signal has been found in the BICEP2/Keck Array data with around 7σ significance, by fitting a freely-floating CMB lensing amplitude in the joint analysis with *Planck* data (BICEP2/Keck Array and Planck Collaborations 2015).

For current or future experiments targeting the detection of primordial *B*-modes, a precise estimation of the secondary CMB *B*-modes at large and intermediate angular scales is required in order to separate the secondary contributions from potential primordial *B*-modes. On the one hand, large angular scale experiments lack the high-resolution *E*-mode measurements that are required to measure the lensing-induced *B*-mode signal. On the other hand, for high-resolution experiments, partial sky coverage limits their ability to extract the *B*-mode power spectrum and to reconstruct the lensing potential at large angular scales. Thus, such experiments would benefit from a pre-estimated secondary *B*-mode template, covering angular scales from a few degrees down to sub-degree scales and matching their sky coverage.

We present an all-sky secondary *B*-mode template spanning from intermediate to large angular scales, synthesized using the full mission *Planck* data. In Planck Collaboration XV (2016), the lensing *B*-mode estimate was band-limited to $\ell > 100$, in order to conservatively alleviate any low-ℓ systematic effects. In contrast, here the focus is on improving the reliability at intermediate angular scales ($10 < \ell < 200$). We also extend the lensing *B*-mode results of Planck Collaboration XV (2016) by producing a lensing *B*-mode map, by performing extensive characterization and robustness tests of this template map and by discussing its utility for *B*-mode oriented experiments. This *B*-mode map is delivered as part of the *Planck* 2015 data release.

The outline of this paper is as follows. Section 2 describes the data and simulations that we use. We detail the methodology for the template synthesis in Sect. 3, and describe the construction of the mask in Sect. 4. The lensing *B*-mode template reconstruction method is validated using simulations in Sect. 5. We present the template we have obtained from *Planck* foreground-cleaned data in Sect. 6, and assess its robustness against foreground contamination and the choice of the data to cross-correlate with in Sect. 7. Section 8 addresses the implications of the template for external experiments targeting primordial *B*-mode searches. We summarize and conclude in Sect. 9.

2. Data and simulations

Planck sky maps: we have used foreground-cleaned CMB temperature and polarization maps derived from the *Planck* satellite full mission frequency channel maps from 30 to 857 GHz in temperature and 30 to 353 GHz in polarization (Planck Collaboration I 2016; Planck Collaboration II 2016; Planck Collaboration III 2016; Planck Collaboration IV 2016; Planck Collaboration V 2016; Planck Collaboration VI 2016; Planck Collaboration VII 2016; Planck Collaboration VIII 2016). Our main results are based on Stokes *I*, *Q*, and *U* maps constructed using the SMICA component-separation algorithm (Delabrouille et al. 2003) in temperature and polarization simultaneously (Planck Collaboration IX 2016). The maps are at $5'$ resolution in $N_{side} = 2048$ HEALPix pixelization (Górski et al. 2005)[2]. For the sake of assessing the robustness of our results, we have also utilized foreground-cleaned maps that are produced using the other *Planck* component-separation methods, namely Commander, NILC, and SEVEM (Planck Collaboration XII 2014; Planck Collaboration IX 2016; Planck Collaboration X 2016). The current publicly available *Planck* HFI polarization maps, which are part of the *Planck* 2015 data release, are high-pass filtered at $\ell \lesssim 30$ because of residual systematic effects on angular scales greater than 10° (Planck Collaboration VII 2016; Planck Collaboration VIII 2016). However, we have used polarization

---

[2] http://healpix.jpl.nasa.gov

maps covering all angular scale for our analysis, since the results have proved not to be sensitive to CMB *E*-mode polarization at large angular scales[3].

Full Focal Plane simulations: for methodological validation and for the bias correction of the lensing potential at the map level (known as the "mean-field" correction), we have relied on the eighth *Planck* Full Focal Plane (FFP8 hereafter) suite of simulations, as described in Planck Collaboration XII (2016). Specifically, we have used FFP8 Monte-Carlo realizations of the Stokes *I*, *Q*, and *U* outputs of the SMICA component-separation method. These have been obtained by processing through the SMICA algorithm the simulated beam-convolved CMB and noise realizations of the nine *Planck* frequency channels, as described in Planck Collaboration IX (2016). As a result, both the noise realizations and the beam transfer function are representative of those of the SMICA foreground-cleaned maps. Finally, the calibration of the *Planck* 2015 data has been taken into account by rescaling the CMB realizations as in Planck Collaboration XV (2016).

Fiducial cosmology: for normalizing the lensing potential map estimate and computing the filter and transfer functions of the *B*-mode template, we have used fiducial power spectra derived from the 2015 *Planck* base ΛCDM cosmological parameters that have been determined from the combination of the 2015 temperature and "lowP" likelihoods, as described in Planck Collaboration XIII (2016).

3. *B*-mode map reconstruction

3.1. Formalism

The secondary *B*-modes of CMB polarization arise from a leakage of a fraction of the *E*-modes into *B*-modes due to the polarization remapping induced by the CMB lensing effect. In terms of the polarization spin-two components $_{\pm 2}P \equiv Q \pm iU$, and at first order in the lensing potential ϕ, the lensing-induced contribution reads

$$_{\pm 2}P^{\text{lens}}(\hat{\boldsymbol{n}}) = \nabla_{\pm 2}P^{\text{prim}}(\hat{\boldsymbol{n}}) \cdot \nabla\phi(\hat{\boldsymbol{n}}), \qquad (1)$$

where $_{\pm 2}P^{\text{prim}}(\hat{\boldsymbol{n}})$ are the polarization fields that would be observed in the absence of the lensing effect (Zaldarriaga & Seljak 1998; Lewis & Challinor 2006). Rewriting the secondary polarization fields in terms of the rotationally invariant *E*- and *B*-mode fields, so that

$$_{\pm 2}P^{\text{lens}}(\hat{\boldsymbol{n}}) = \nabla\left[\sum_{\ell' m'}\left(E_{\ell' m'}^{\text{prim}} \pm iB_{\ell' m'}^{\text{prim}}\right)_{\pm 2}Y_{\ell' m'}\right] \cdot \nabla\phi(\hat{\boldsymbol{n}}), \qquad (2)$$

and considering their spin-two spherical-harmonic coefficients

$$_{\pm 2}P_{\ell m}^{\text{lens}} = \int d\hat{\boldsymbol{n}} \ _{\pm 2}P^{\text{lens}}(\hat{\boldsymbol{n}}) \ _{\pm 2}Y_{\ell m}^*(\hat{\boldsymbol{n}}), \qquad (3)$$

one finds that the gradient-free *B*-mode polarization receives a secondary contribution that depends on the primordial *B*-modes and the unlensed curl-free *E*-modes, of the form

$$B_{\ell m}^{\text{lens}} = \frac{1}{2i}\left(_{+2}P_{\ell m}^{\text{lens}} -_{-2}P_{\ell m}^{\text{lens}}\right). \qquad (4)$$

---

[3] The *E*-mode polarization at $\ell < 30$ contributes only at the sub-percent level to the template-based lensing *B*-mode power spectrum at $\ell = 10$, and has even lower contribution at higher multipoles.

3.2. Algorithm

First, we state the assumptions on which our algorithm is based. Since the *E*-mode amplitude is at least an order of magnitude greater than the primordial *B*-mode amplitude, the $B_{\ell m}^{\text{lens}}$ contribution that comes from the *E*-mode remapping largely dominates over the one from the lensing perturbation of the primordial *B*-modes. From now on, the latter can safely be neglected, consistent with the assumptions in Planck Collaboration XV (2016). We replace the primordial *E*-modes that appear in Eq. (2) with the total *E*-modes, $E = E^{\text{prim}} + \delta E$. This amounts to neglecting the second-order contribution to B^{lens} due to δE, that is to say the lensing perturbation of the *E*-modes themselves.

We then consider pure *E* polarization fields:

$$_{\pm 2}P^E(\hat{\boldsymbol{n}}) \equiv Q^E(\hat{\boldsymbol{n}}) + iU^E(\hat{\boldsymbol{n}}) \equiv \sum_{\ell m} E_{\ell m} \ _{\pm 2}Y_{\ell m}(\hat{\boldsymbol{n}}), \qquad (5)$$

which define pure-*E* Stokes parameters Q^E, U^E.

Implementing the above assumptions into Eq. (3) and using the definition given in Eq. (5), we build a secondary polarization estimator that has the generic form

$$_{\pm 2}\hat{P}_{\ell m}^{\text{lens}} = \mathcal{B}_{\ell}^{-1} \int d\hat{\boldsymbol{n}} \ \nabla_{\pm 2}\widetilde{P^E}(\hat{\boldsymbol{n}}) \cdot \nabla\widetilde{\phi}(\hat{\boldsymbol{n}}) \ _{\pm 2}Y_{\ell m}^*(\hat{\boldsymbol{n}}), \qquad (6)$$

where $_{\pm 2}\widetilde{P^E}$ and $\widetilde{\phi}$ are the filtered versions of the pure-*E* polarization and lensing potential fields, respectively, whereas $\mathcal{B}_{\ell}$ is a transfer function ensuring that the estimator is unbiased. These quantities are defined below in Sect. 3.4. We finally define secondary CMB *B*-mode template Stokes maps $(Q^{\text{lens}}(\hat{\boldsymbol{n}}), U^{\text{lens}}(\hat{\boldsymbol{n}}))$ by preserving the *B*-mode contribution in Eq. (6) and transforming back to real space.

In summary, we reconstruct the all-sky *B*-mode template using a dedicated pipeline that consists of:

(i)   estimation of the deflection field using the filtered reconstructed gravitational potential, $\nabla\widetilde{\phi}(\hat{\boldsymbol{n}})$;
(ii) computation of the gradient of the filtered pure *E*-mode input maps, $\nabla_{\pm 2}\widetilde{P^E}(\hat{\boldsymbol{n}})$;
(iii) calculation of the analytical transfer function;
(iv) construction of the polarization template using Eq. (6);
(v)   formation of a secondary *B*-mode template using Eq. (4).

These steps are further detailed in the rest of this section.

3.3. All-sky lensing potential reconstruction

The paths of CMB photons are weakly deflected by the matter encountered along the way from the last-scattering surface. As a result, the primary CMB observables are remapped according to the gradient of the gravitational potential ϕ integrated along the line-of-sight (Blanchard & Schneider 1987). This induces higher-order correlations within the CMB observables; namely, a non-vanishing connected part of the four-point correlation function, or equivalently in the spherical harmonic domain, a trispectrum, in the CMB maps. These can be used, in turn, to reconstruct the intervening mass distribution (Bernardeau 1997; Zaldarriaga & Seljak 1999). Specifically, to first order in ϕ, the lensing induces a correlation between the observed (lensed) CMB maps and the gradient of the primary (unlensed) maps. Building upon this property, quadratic estimators have been proposed to extract a lensing potential estimate from the observed map (Hu 2001b,a; Hu & Okamoto 2002; Okamoto & Hu 2003). We have reconstructed the lensing potential over a large portion of the sky using the all-sky quadratic estimator described

-5.0 ▮▮▮▮▮▮ 5.0
$\times 10^{-5}$
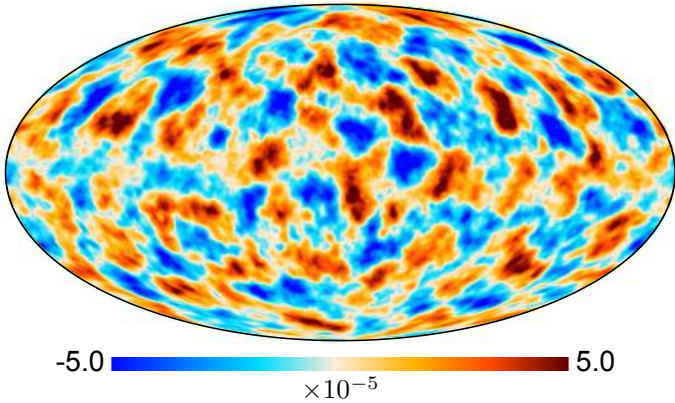
Fig. 1. Wiener-filtered lensing potential estimated from the `SMICA` foreground-cleaned temperature map using the $f_{\rm sky} \simeq 80\%$ lensing mask. The lensing potential estimate, which is shown in Galactic coordinates, is effectively inpainted using a lensing extraction method that relies on an inpainting of the input temperature map, as discussed in Sect. 3.3.1.

in Okamoto & Hu (2003), which has been modified to deal with cut skies.

3.3.1. Inpainting of the temperature map

In Planck Collaboration XV (2016), foreground-contaminated regions have been masked out at the stage of the inverse-variance filtering of the input CMB maps, by allocating infinite variance to masked pixels. The reconstructed ϕ is thus null-valued in the pixels inside the analysis mask. For the sake of synthesizing Stokes maps ($Q^{\rm lens}(\hat{n})$, $U^{\rm lens}(\hat{n})$), as described in Sect. 3.2, using such a masked ϕ estimate would induce prohibitive amounts of mode mixing. Thus, we have used the `METIS` method, in which the masked CMB maps are restored to a complete sky coverage, before their ingestion into the quadratic estimator, by means of an inpainting procedure based on the "sparsity" concept (Abrial et al. 2007). More details are given in Perotto et al. (2010), where this method has been first described and in Planck Collaboration XVII (2014), where it has been used to perform consistency tests. As a result of this procedure, the `METIS` method provides a ϕ estimate that is effectively inpainted to cover the full sky. To illustrate this property, Fig. 1 shows a Wiener-filtered version of the ϕ estimate reconstructed from the `SMICA` temperature map using the baseline "L80" lensing mask that we describe below in Sect. 4.

As well as offering the advantage of mitigating the bias that the mask induces in the ϕ map, which is discussed in Sect. 3.3.2, this allows us to construct the secondary polarization template map using Eq. (6), alleviating the need for further processing steps to deal with partial sky coverage.

3.3.2. Mean-field debiasing

The quadratic estimator is based on the fact that, for a fixed lens distribution, the lensing breaks the statistical isotropy of the CMB maps; specifically, it introduces off-diagonal terms of the CMB covariance (Hu & Okamoto 2002). Therefore this is also sensitive to any other source of statistical anisotropies in the maps. For *Planck* data, the bias induced at the ϕ map level by any known sources of statistical anisotropies, which is referred to as the "mean-field bias", is dominated by the effects of masking (Planck Collaboration XVII 2014). The mean-field bias can

be estimated from Monte-Carlo (MC) simulations that include all the instrumental and observational effects that can lead to a sizeable mean-field (e.g. the mask, the spatial inhomogeneity in the noise, which yields the first sub-dominant mean field, and the beam asymmetry), by averaging the ϕ estimates obtained on MC realizations. We have used a set of 100 FFP8 realizations to obtain an estimate $\langle\bar{\phi}_{\rm LM}\rangle_{\rm MC}$ of the mean-field modes[4] for the non-normalized ϕ modes, labelled $\bar{\phi}_{\rm LM}$. This mean-field estimate has then been subtracted from $\bar{\phi}$ to obtain the unbiased estimate $\hat{\phi}_{\rm LM}$ of ϕ in the spherical harmonic domain, given by

$$\hat{\phi}_{\rm LM} = \mathcal{A}_{\rm L}\left(\bar{\phi}_{\rm LM} - \langle\bar{\phi}_{\rm LM}\rangle_{\rm MC}\right), \qquad (7)$$

where $\mathcal{A}_{\rm L}$ is the normalization function, which ensures that the estimator is unbiased. This is related to the normalization $A_{\rm L}^{\alpha}$ given in Okamoto & Hu (2003)[5], via $\mathcal{A}_{\rm L} = [L(L+1)]^{-1}A_{\rm L}^{\alpha}$, and has been analytically calculated using the fiducial cosmology described in Sect. 2. To handle the slight difference between FFP8 input cosmology and the fiducial cosmology considered here, the mean-field $\langle\bar{\phi}_{\rm LM}\rangle_{\rm MC}$ has been multiplied by the ratio of the normalization functions derived from the input FFP8 and fiducial cosmological models.

3.3.3. Mass tracer choice

In addition to the lensing potential quadratic estimate, other tracers of the underlying lensing potential could be used to form a lensing-induced *B*-mode template. The cosmic infrared background (CIB) emission is of particular interest for this purpose since, in contrast to most of the large-scale structure tracers, which probe only a limited range of redshifts; its redshift distribution has a broad overlap with the lensing potential kernel (Song et al. 2003). Using the best-fit halo-based model of Planck Collaboration XVIII (2011), Planck Collaboration XVIII (2014) have reported a roughly 80% correlation of the CIB fluctuations measured by *Planck* with the lensing potential, in agreement with the model expectations. For the sake of the lensing *B*-mode measurement, however, the uncertainties in the CIB modelling will have a large impact on the signal estimate, unless the CIB model parameters are marginalized within a joint analysis including lensing cross- and auto-power spectrum measurements of the CIB (Sherwin & Schmittfull 2015). Moreover, the foreground residuals are another concern for any lensing *B*-mode template synthesized from the CIB, as also discussed in Sherwin & Schmittfull (2015). The CIB signal is the most precisely measured at high frequencies, where the Galactic dust emission is also important. Any Galactic dust residuals in the CIB template map could be correlated either with the polarized dust residuals or with the intensity-to-polarization leakage of the dust emission in the CMB *E*- and *B*-mode maps.

Similarly, lensing potential estimates can also be extracted by means of a quadratic estimator on the *Planck* polarization maps. This, combined with the temperature-based ϕ estimate, reduces the power spectrum of the ϕ reconstruction noise by roughly 25%. However, for measuring the lensing *B*-mode power spectrum using a template-based approach, resorting to a polarization-based ϕ estimate would require us to correct for a non-negligible Gaussian bias (Planck Collaboration XV 2016; Namikawa & Nagata 2014).

---

[4] We use multipole indices LM for the lensing potential in order to differentiate them from the ℓm indices used for the CMB fields.

[5] It is also related to the response function of the quadratic estimator for off-diagonal terms of the CMB covariance $\mathcal{R}_{\rm L}$, as defined in Eq. (A.16) of Planck Collaboration XV (2016), via $\mathcal{A}_{\rm L} = \mathcal{R}_{\rm L}^{-1}$.

Here we have chosen to employ only the lensing potential estimate to produce a lensing *B*-mode template that is model-independent and more robust to foreground residuals; and to use the temperature data only for estimating the lensing potential, which ensures desirable properties for our template, as discussed in Sect. 5. Relying on the independent analysis presented in Planck Collaboration XV (2016), we show in Sect. 7.4 that these choices induce at worst a marginal increase in the statistical uncertainties of the lensing *B*-mode measurements.

3.4. Lensing-induced polarization fields

Using the lensing potential estimate discussed above and the observed *E*-mode map, we have reconstructed the template of the secondary polarization field as in Eq. (6). To reduce uncertainties, we have used filtered versions of those maps that are defined as

$$\widetilde{\phi}(\hat{\boldsymbol{n}}) = \int \mathrm{d}\hat{\boldsymbol{n}} \; f_{\mathrm{L}}^{\phi} \; \hat{\phi}_{\mathrm{LM}} \, Y_{\mathrm{LM}}^{*}(\hat{\boldsymbol{n}}), \tag{8}$$

and

$$_{\pm 2}\widetilde{P^{E}}(\hat{\boldsymbol{n}}) = \int \mathrm{d}\hat{\boldsymbol{n}} \; f_{\ell}^{E} \, E_{\ell m} \, _{\pm 2}Y_{\ell m}^{*}(\hat{\boldsymbol{n}}). \tag{9}$$

The filter functions for ϕ and E, f_{L}^{ϕ} and f_{ℓ}^{E}, are Wiener filters, based on the optimality arguments developed in Smith et al. (2009a). In Planck Collaboration XV (2016), the ϕ estimates at $L < 8$ have been discarded because of instability to the choice of the method used to correct the mean-field. Consistently, we have filtered the ϕ estimate to $L \leq 10$ in order to conservatively avoid any mean-field related issues. We have used a tapering filter, labelled f_{10}, that smoothly goes from zero at $L = 5$ to unity at $L = 15$ by means of a power-of-cosine function centred in $L = 10$. Using this filter, we still preserve 99% of the available information for measuring the cross-correlation *B*-mode power spectrum. The filtered pure-*E* polarization fields $_{\pm 2}\widetilde{P^{E}}$ have been directly obtained from the full-sky observed *Q* and *U* maps by transforming into the spin-weighted spherical harmonic basis, filtering the *E*-modes, and reforming Stokes parameter fields with a null *B*-mode component. No deconvolution of the beam has been performed at this stage, which yields further filtering of the *E*-modes at high multipoles. Our filtering functions are defined by

$$f_{\mathrm{L}}^{\phi} = \frac{f_{10} C_{\mathrm{L}}^{\phi,\mathrm{fid}}}{C_{\mathrm{L}}^{\phi,\mathrm{fid}} + N_{\mathrm{L}}^{\phi}},$$

$$f_{\ell}^{E} = \frac{C_{\ell}^{E,\mathrm{fid}}}{C_{\ell}^{E,\mathrm{fid}} + N_{\mathrm{L}}^{E}}, \tag{10}$$

where C_{L}^{ϕ} and C_{ℓ}^{E} are the fiducial ϕ and *E*-mode power spectra; N_{L}^{ϕ} is the ϕ reconstruction noise power spectrum calculated following Okamoto & Hu (2003); and N_{L}^{E} is the pixel- and beam-deconvolved power spectrum of the *E*-mode noise.

These steps have been performed using the fast spin-weighted spherical harmonic transform capability of the `HEALPix` library to generate Q^{E} and U^{E} and compute their derivatives. Thanks to this simple implementation, a *B*-mode template map at a resolution of 5′ can be reconstructed from the ϕ estimate and the observed *Q* and *U* maps in a reasonable amount of computing time, which enables the use of Monte-Carlo simulations. For example, the computing time is about

two minutes using eight cores of the Linux AMD64 machines of the Institut National de Physique Nucléaire et de Physique des Particules (IN2P3) Computing Center[6].

Using a harmonic approach, as in Hu (2000), we compute the transfer function that appears in Eq. (6) by imposing the condition that the secondary *B*-mode template $\hat{B}^{\mathrm{lens}} \equiv (_{+2}\hat{P}^{\mathrm{lens}} - _{-2}\hat{P}^{\mathrm{lens}})/(2\mathrm{i})$ satisfies

$$\langle B_{\ell m}^{*} \hat{B}_{\ell' m'}^{\mathrm{lens}} \rangle = \delta_{\ell \ell'} \delta_{mm'} \, C_{\ell}^{B,\mathrm{fid}}, \tag{11}$$

where $C_{\ell}^{B,\mathrm{fid}}$ is the fiducial lensing-induced *B*-mode power spectrum ($r = 0$).

In terms of the fiducial power spectra $C_{\ell}^{X,\mathrm{fid}}$, $X = \{E, B, \phi\}$, we obtain a transfer function

$$\mathcal{B}_{\ell} = \frac{1}{C_{\ell}^{B,\mathrm{fid}}} \sum_{\mathrm{L}\ell'} f_{\mathrm{L}}^{\phi} C_{\mathrm{L}}^{\phi,\mathrm{fid}} \, f_{\ell'}^{E} B_{\ell'} C_{\ell'}^{E,\mathrm{fid}} \, _{2}F_{\ell\mathrm{L}\ell'}, \tag{12}$$

where $B_{\ell'}$ is the beam function of the polarization maps, and $_{2}F_{\ell\mathrm{L}\ell'}$ is a geometrical term defined in Hu (2000).

3.5. B-mode template synthesis

Our secondary *B*-mode template is obtained as in Eq. (4) that is

$$\hat{B}_{\ell m}^{\mathrm{lens}} = \frac{1}{2\mathrm{i}} \left(_{+2}\hat{P}_{\ell m}^{\mathrm{lens}} - _{-2}\hat{P}_{\ell m}^{\mathrm{lens}} \right). \tag{13}$$

This is computed from $_{+2}\hat{P}_{\ell m}^{\mathrm{lens}}$, the spin-weighted spherical harmonic transforms of our real-space secondary polarization estimates $\left(Q^{\mathrm{lens}} \pm \mathrm{i} U^{\mathrm{lens}} \right)$ that are corrected for the transfer function given in Eq. (12).

3.6. Cross-correlation power spectrum of the template

We form the cross-correlation power spectrum between the template *B*-modes given in Eq. (13) and the observed *B*-modes, $B_{\ell m}^{\mathrm{obs}}$, using

$$\hat{C}_{\ell}^{BB^{\mathrm{lens}}} = \frac{1}{f_{\mathrm{sky}}^{\mathrm{eff}}(2\ell + 1)} \sum_{m=-\ell}^{\ell} B_{\ell m}^{\mathrm{obs}\,*} \tilde{B}_{\ell m}^{\mathrm{lens}}, \tag{14}$$

where the asterisk denotes complex conjugation; and $\tilde{B}_{\ell m}^{\mathrm{lens}}$ is a shorthand notation for the template *B*-mode harmonic coefficients obtained as in Eq. (12), but using an apodized and masked version of the real-space secondary polarization estimates $\left(Q^{\mathrm{lens}} \pm \mathrm{i} U^{\mathrm{lens}} \right)$. This apodized mask, the construction of which is described in Sect. 4, leaves an effective available sky fraction $f_{\mathrm{sky}}^{\mathrm{eff}}$ for analysis. The BB^{lens} cross-correlation power spectrum represents an estimate of the lensing *B*-mode power spectrum. Moreover, this does not require any noise term subtraction, as we verify in Sect. 5.

The BB^{lens} power spectrum variance is estimated to a good approximation using

$$\sigma^{2}\left(\hat{C}_{\ell}^{BB^{\mathrm{lens}}} \right) = \frac{1}{f_{\mathrm{sky}}^{\mathrm{eff}}(2\ell + 1)} \left[(C_{\ell}^{B})^{2} + (\hat{C}_{\ell}^{B^{\mathrm{obs}}})(\hat{C}_{\ell}^{B^{\mathrm{lens}}}) \right], \tag{15}$$

where $\hat{C}_{\ell}^{B^{\mathrm{obs}}}$ is the auto-correlation power spectrum of the observed *B*-modes and $\hat{C}_{\ell}^{B^{\mathrm{lens}}}$ the one of the template. Equation (15) consists of a Gaussian variance prescription

---

6 http://cc.in2p3.fr/?lang=en

(see e.g. Knox 1995), which is not expected to rigorously apply to the lensing *B*-mode power spectrum estimate, because of its "sub-structure" (since it is based on the sum of the $TTEB$ trispectrum of the observed CMB signal). However, for a template map constructed on the *Planck* polarization maps, given the polarization noise level, the higher-order terms that enter the variance are sub-dominant, as is further discussed and tested in Sect. 5.

4. Construction of the *B*-mode mask

In this section, we detail the methodology for constructing the template mask. This has involved first preparing a series of foreground masks targeted at specific foreground emission in temperature. These foreground masks have been then combined to construct an analysis mask for the lensing potential reconstruction. Finally, the lensing analysis mask has been modified to define a mask for the template map. These three steps are detailed in Sects. 4.1–4.3 below.

4.1. Foreground masks

Galactic mask

We have masked the regions of the sky that are strongly contaminated by the diffuse Galactic emission, the carbon-monoxide (CO) transition line emission and the extended nearby galaxy emission. This Galactic mask has been produced following the method described in Planck Collaboration XVI (2014). It includes the diffuse Galactic mask described in Planck Collaboration XII (2014), which is produced by thresholding a combination of CMB-corrected temperature maps at 30 and 353 GHz until a desired sky fraction is preserved. For our baseline analysis, we have used a diffuse Galactic mask that retains about 80% of the sky. This diffuse Galactic mask discards mainly low latitude regions. To mask the CO lines contamination at intermediate latitudes, we have used the CO mask described in Appendix A of Planck Collaboration XI (2016), which has been obtained by thresholding a smoothed version of the Type 3 CO map (Planck Collaboration XIII 2014) at $1 \, \mathrm{K_{RJ} \, km \, s^{-1}}$. Furthermore, we have removed the emission from the most extended nearby galaxies, including the two Magellanic clouds (LMC, SMC) and M 31, by cutting a radius that covers each galaxy in the 857-GHz map, as described in Planck Collaboration XI (2016). Our Galactic mask, which is the merge of the diffuse Galactic, CO-line, and extended nearby galaxy masks, consists of large cuts that extend over more than two degrees on the sky, and preserves 79% of the sky.

Extragalactic object masks

We have masked the infrared (IR) and radio point sources that have been detected in the temperature maps in frequency channels from 70 to 353 GHz using the *Planck* compact object catalogues, as well as the sky areas contaminated by the Sunyaev-Zeldovich (SZ) emission using both *Planck* SZ cluster catalogues and Compton parameter maps. We started with the individual masks targeted at 100, 143, and 217 GHz that have been used in Planck Collaboration XVII (2014). These masks have been produced using the *Planck* Early Release Compact Source Catalogue (ERSC; Planck Collaboration VII 2011), the *Planck* Catalogue of Compact Sources (PCCS; Planck Collaboration XXVIII 2014), and the *Planck* catalogue of Sunyaev-Zeldovich

sources (PSZ; Planck Collaboration XXIX 2014). These have been merged with the conservative point-source masks produced using the 2015 catalogue (PCCS2; Planck Collaboration XXVI 2016), which are presented in Planck Collaboration XI (2016). The SZ emission hav been further removed using the template Compton parameter y map for the detected galaxy clusters of the 2015 SZ catalogue (PSZ2; Planck Collaboration XXVII 2016) that is described in Planck Collaboration XXII (2016). Individual SZ masks have been constructed for 100, 143, and 217 GHz separately, by converting the template y-map into CMB temperature using the corresponding conversion factors listed in Planck Collaboration XXII (2016), and thresholding at $10 \, \mu\mathrm{K}$. Finally, we have masked several small nearby galaxies including M 33, M 81, M 82, M 101, and CenA, as described in Planck Collaboration XI (2016).

We have combined these individual masks to produce two extragalactic object masks that differ in the maximum cut radius. First, the "extended object mask" is made of holes the largest angular size of which ranges from two degrees to 30′. This includes the extended SZ clusters and the small nearby galaxies. Second, the "compact object mask" is a collection of small holes of cut radius smaller than 30′, and comprises the detected radio and IR point sources and the point-like SZ clusters. The latter represents a conservative point source mask that includes all the point sources detected above $S/N = 5$ in the 100-, 143-, and 217-GHz maps, as well as the point sources detected above $S/N = 10$ in the adjacent frequencies (including 70 and 353 GHz). This has been used in Sect. 7.2 to test the robustness of our results agaadts point source residuals in the SMICA map.

4.2. Lensing analysis mask

For the lensing potential reconstruction, we have prepared a composite mask targeted at the SMICA temperature map. This map comes along with a "confidence" mask that defines the sky areas where the CMB solution is trusted. The SMICA confidence mask, a thorough description of which is given in Planck Collaboration IX (2016), has been produced by thresholding the CMB power map that is obtained in squaring a band-pass filtered and smoothed version of the SMICA map. Our lensing mask combines the Galactic, extended, and compact object masks after some changes driven by the SMICA confidence mask. Namely, the LMC and three molecular clouds at medium latitudes have been masked more conservatively in the SMICA mask than in our initial Galactic mask. We have enlarged the latter accordingly. In the compact object mask, IR and radio source holes that are not also present in the SMICA confidence mask have been discarded. They mainly corresponds to point sources detected in the 353-GHz map, and are strongly weighted down in the SMICA CMB map. The modified compact object mask removes 0.6% of the sky in addition to the 21.4% Galactic and the 0.4% extended object cuts. The baseline lensing mask, which consists of the combination of these three masks, retains 77.6% of the sky and is labelled L80.

In Sect. 7.2, however, we test the stability of our results against source contamination by using a mask accounting for more point-like and extended sources. This has been constructed as the union of the Galactic, extended, and compact objects and SMICA confidence masks. This mask, in which the cut sky fraction due to point sources is as large as 1.5%, preserves 76% of the sky for analysis and is named L80s.

4.3. Template analysis mask

4.3.1. Methodology for constructing the mask

Given the lensing mask, the construction of the template mask is a trade-off between preserving a large sky fraction for analysis and alleviating the bias induced by the lensing reconstruction on an incomplete sky. Inpainting the masked temperature map from which the lensing potential is extracted, as described in Sect. 3.3, strongly suppresses this effect. The point-like holes induce negligible bias in the lensing potential reconstruction provided they are treated by inpainting beforehand (Benoit-Lévy et al. 2013). Therefore, the compact object mask does not need to be propagated to the template map, as it is verified using Monte-Carlo simulations in Sect. 5. However, larger sky cuts performed by the lensing mask (e.g., those arising from the Galactic and extended object masks) have to be applied to the *B*-mode template. Furthermore, some artefacts may be seen near the mask boundaries, which we refer to as the mask leakage, and which arises from the convolution of the signal with the mask side-lobes when transforming in spherical harmonic space (Plaszczynski et al. 2012). From these considerations, we have tailored a method of constructing the mask template using Monte-Carlo simulations: starting with the combination of the Galactic and the extended object masks, we progressively enlarged the mask beyond the boundaries, until we observed a negligible residual bias in the cross-correlation power spectrum of the template. This has been obtained by extending the Galactic mask 3° beyond the boundaries and the extended compact object mask 30′ beyond. In Sect. 5, we check that using a template mask that are constructed in this fashion allows no significant impact in the BB^{lens} lensing *B*-mode power spectrum.

4.3.2. The baseline and test template masks

The baseline mask of the lensing *B*-mode template map has been constructed from the lensing analysis L80 mask using the method described above. Specifically, the Galactic mask has been enlarged 3° beyond the boundaries, removing 30% of the sky, and the extended object mask has been also slightly widened by 30′ beyond the boundaries, removing an additional 1.2% of the sky. The baseline template mask preserves a sky fraction of 69% and is named B70.

In Sect. 7.2, however, we check that consistent results are obtained using either the Galactic mask as it is, without enlargement, or a more conservative Galactic mask that removes 40% of the sky. The most aggressive template mask, labelled B80, leaves 77% of the sky for the analysis, and the most conservative one, named B60, leaves 58%. We also test against extragalactic contamination through using the lensing L80s mask for the lensing potential reconstruction and the corresponding template mask constructed using the method described in Sect. 4.3.1 and labelled B70s. In addition to these masks that are targeted at the temperature map, in Sect. 7.2, we also use a mask tailored for polarization in order to test against polarized foreground contamination. For this purpose, the B70 mask has been combined with the SMICA confidence mask for polarization, a detailed description of which is given in Planck Collaboration IX (2016). The latter removes regions of the sky where the polarization power (which is computed by squaring a low-pass filter-smoothed version of the SMICA polarization map) exceeds $5\,\mu\mathrm{K}^2$. The combined B70 and SMICA confidence mask for polarization is labelled B70p and retains 68% of the sky.

Table 1. Template analysis masks.

Mask label	f_{sky}	$f_{\mathrm{sky}}^{\mathrm{eff}}$
B60	0.58	0.54
B70	0.69	0.65
B70p	0.68	0.64
B70s	0.68	0.61
B80	0.77	0.69

Notes. The columns labelled f_{sky} and $f_{\mathrm{sky}}^{\mathrm{eff}}$ give the sky fractions that are preserved by the masks and their apodized versions, respectively.

When computing the lensing *B*-mode power spectrum, we have employed apodized versions of the masks, using a cosine taper of 2° width for the Galactic mask and 30′ width for the extended object mask. As a consequence, effective sky fractions available for the power spectrum are 5–10% lower than the sky fraction of the template analysis masks. A list of the template masks discussed here is given in Table 1, together with the corresponding sky fraction, both with and without apodization.

5. Validation on simulations

We now validate the pipeline described in Sect. 3 and test the impact of masking as described in Sect. 4.3 using a Monte-Carlo (MC) approach. We analyse our template by forming the BB^{lens} power spectrum given in Eq. (14), which has two objectives:

(i) to assess that the template encloses the expected lensing *B*-mode information, thus validating the assumptions on which the synthesis method relies;
(ii) to demonstrate its utility for measuring the secondary *B*-mode power spectrum.

We use two independent sets of 100 SMICA *I*, *Q*, and *U* simulations, part of the FFP8 MC simulation set described in Sect. 2.

5.1. Full-range power spectrum estimate

We have applied the pipeline described above to the SMICA temperature and Stokes parameter simulations to obtain a set of 100 $\hat{B}^{\mathrm{lens}}$ estimates. For the lensing reconstruction on the temperature simulations, we have used the baseline L80 lensing mask, and employed the second simulation set for the mean-field bias correction. Then, lensing *B*-mode power spectrum estimates have been formed by cross-correlating $\hat{B}^{\mathrm{lens}}$ and the input *B*-modes as in Eq. (14), and using the apodized version of the B70 mask. We have estimated the lensing *B*-mode BB^{lens} band-powers by multiplying Eq. (14) by $\ell(\ell+1)/2\pi$ and averaging the multipoles over bins of width $\Delta\ell \geq 100$ to further reduce the pseudo-C_ℓ multipole mixing.

Figure 2 shows the averaged BB^{lens} band-powers obtained using the apodized B70 mask. The error bars have been estimated using the standard deviation of 100 estimates of the BB^{lens} band-powers with the apodized B70 mask. The averaged BB^{lens} band-power residuals, i.e. $\Delta C_b^{BB\mathrm{lens}} = \sum_{\ell\in b} C_\ell^{BB\mathrm{lens}} - C_\ell^{BB,\mathrm{fid}}$, are plotted in the lower panel of Fig. 2; this shows a negligible residual bias of $\lesssim 0.1\sigma$ up to multipoles of 2000. Relative to the input lensing *B*-mode band-power, this corresponds to less than a percent. To isolate the impact of the inpainting, we have also extracted the lensing *B*-modes using the lensing potential reconstructed from the full-sky temperature map, that is without using
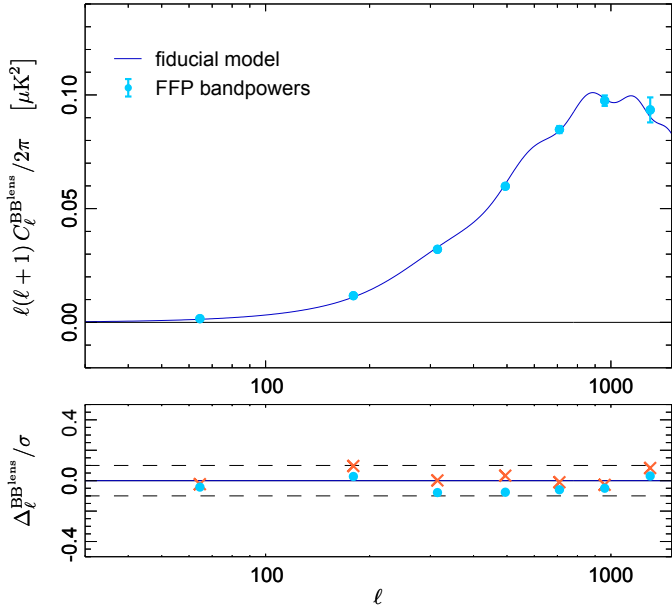
Fig. 2. Lensing B-mode power spectrum obtained by cross-correlating the B^{lens} templates with the corresponding fiducial B-mode simulations (*top*), and residuals with respect to the model (*bottom*). *Top*: averaged BB^{lens} band-powers using the apodized B70 template mask, with multipole bins of $\Delta\ell \geq 100$ (blue points). The error bars are the standard deviation on the mean of the band-power estimate set. The dark blue curve is the fiducial B-mode power spectrum of our simulations, which assumes $r = 0$. *Bottom*: BB^{lens} band-power residual with respect to the fiducial model, given in units of the 1σ error of a single realization. For comparison, we also show the band-power residuals obtained without masking, as discussed in Sect. 5.1 (red points). Dashed lines show the $\pm 1\sigma$ range of 100 realizations, indicating the precision level to which we are able to test against bias.

any mask. For comparison, the band-power residuals are also plotted for full-sky case in Fig. 2.

We have further tested that the BB^{lens} band-powers constitute an unbiased estimate of the fiducial lensing B-modes by fitting an amplitude with respect to the fiducial model. The averaged amplitude $A_{B\mathrm{lens}}$ obtained on 100 estimates of the BB^{lens} band-powers using the B70 mask is 0.989 ± 0.008, where the error has been evaluated using the standard deviation of the $A_{B\mathrm{lens}}$ estimates normalized by the square root of the number of realizations. We therefore conclude that our pipeline provides us with an unbiased estimate of $A_{B\mathrm{lens}}$.

It is worth noting that the choice of extracting the lensing potential from the temperature-only data ensures the absence of Gaussian $N_{\mathrm{L}}^{(0)}$-like bias, which must be corrected for in the case of a lensing extraction using B-mode information. It also gives a strong suppression of any higher-order bias terms.

5.2. Statistical error budget

First, we have quantified the statistical error associated with our lensing B-mode band-power measure via simulations by computing the standard deviation of our MC band-power estimates. Then, these MC error bars have been compared to semi-analytical errors evaluated in taking the square root of the Gaussian variance given in Eq. (15). The auto-correlation B-mode power spectrum of the `SMICA` simulation has been modelled using $C_\ell^{B^{\mathrm{obs}}} = C_\ell^B + B_\ell^{-2} N_\ell^B$, where C_ℓ^B and N_ℓ^B are the MC input signal and noise power spectra and B_ℓ is the beam function.
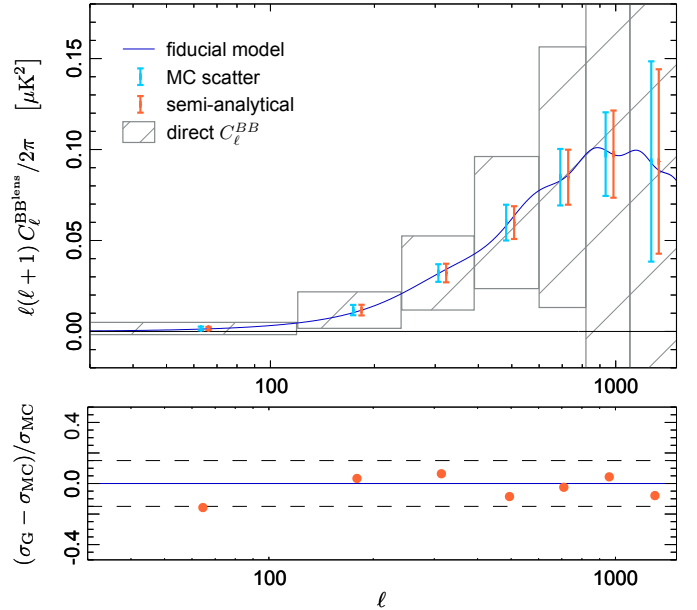
Fig. 3. Error budget. We compare the MC derived uncertainties σ_{MC} associated with the BB^{lens} measurements to the semi-analytical errors σ_{G} obtained using Eq. (15). *Top*: averaged BB^{lens} band-powers using either σ_{MC} (blue) or σ_{G} (red) as error estimates. For illustration, we also show the expected sensitivity of the *Planck* `SMICA` CMB polarization map to the BB band-powers (grey boxes), whose uncertainties are a factor of four larger than those of the BB^{lens} band-powers using the lensing B-mode template. *Bottom*: relative difference of σ_{G} with respect to σ_{MC}. Dashed lines show a 15% difference.

For the auto-correlation power spectrum of the template, we have used the averaged estimate on our MC set. Furthermore, we have used the $\Delta\ell \geq 100$ binning function to average the variance over multipoles. We note that these large multipole bins contribute to drive our band-power estimates close to a normal distribution by virtue of the central-limit theorem, which in turn, brings the Gaussian variance of Eq. (15) closer to the true variance.

In Fig. 3, we plot the MC error bars and the semi-analytical ones. For comparison purposes, we also show the errors one would have obtained from a BB power spectrum measurement by computing the auto-power spectrum of the fiducial B-mode map.

The uncertainties in our BB^{lens} band-powers are well approximated by the semi-analytical errors at all multipoles. In the lower panel of Fig. 3 we plot the relative difference between the semi-analytical errors using Eq. (15) and the error estimates obtained by simulations. Using Eq. (15) leads to a 16% underestimate of the error in the first multipole bin and less than 10% underestimation at higher multipoles. These results validate the use of Eq. (15) to evaluate the template-based B-mode power spectrum uncertainties. We also find that the uncertainties of the BB^{lens} power spectrum using the template map are approximately four times lower than those of a total B-mode BB measurement coming directly from the B-mode map.

Gathering the results of our MC analysis, we observe that, when used in cross-correlation with the B-mode map, the lensing B-mode template we compute provides a lensing C_ℓ^B measurement, which: (i) does not rely on any bias subtraction; (ii) has nearly optimal uncertainty; and (iii) has four times lower uncertainty than the BB measurement on the fiducial B-mode map.
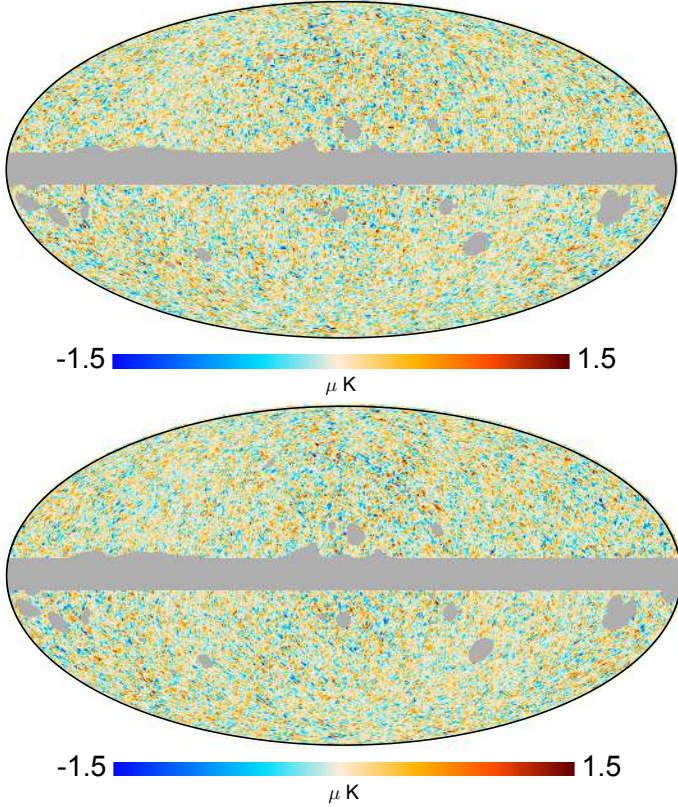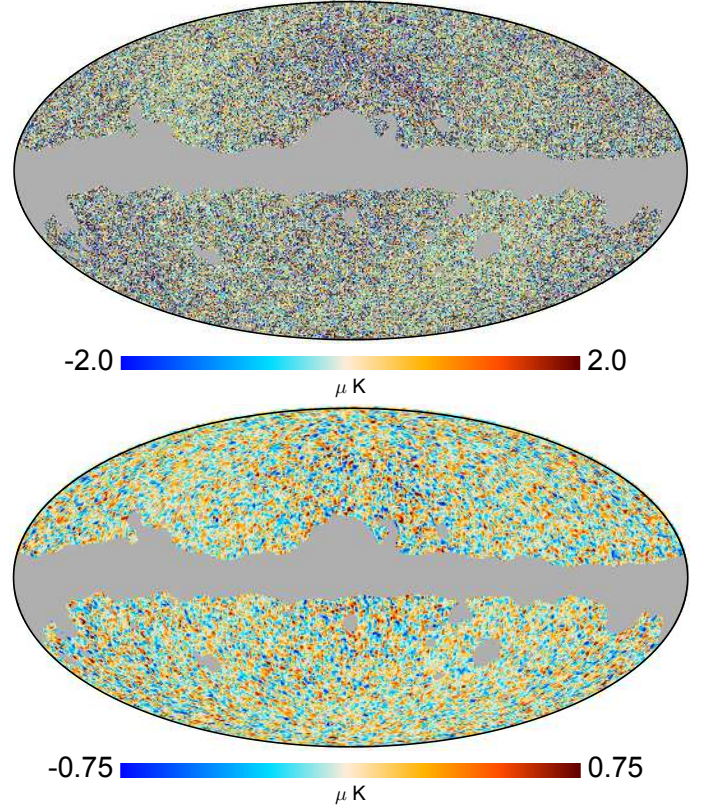
Fig. 4. `SMICA` lensing-induced *Q* and *U* templates that have been convolved with a Gaussian beam of 60′ *FWHM* to highlight the large angular scales (corresponding to multipoles below 200). No spurious patterns are observed at large angular scales.

Fig. 5. *Planck*-derived *B*-mode template map computed using the `SMICA` foreground-cleaned CMB maps. For illustration, the map has been convolved with a Gaussian beam of 10′ (*upper panel*) and 60′ (*lower panel*) *FWHM*. The grey area represents the L80 mask, which was used at the lensing potential reconstruction stage. No obvious foreground residuals are seen in the high-resolution map, nor any obvious systematic effects in the low-resolution one.

6. *Planck*-derived secondary *B*-mode template

6.1. Template synthesis

We have produced the template map of the lensing *B*-modes by applying the pipeline described in Sect. 3 to the foreground-cleaned temperature and polarization maps obtained using the `SMICA` component-separation method, as described in Sect. 2. We have first obtained the $\hat{Q}^{\text{lens}}$ and $\hat{U}^{\text{lens}}$ templates defined in Sect. 3.2, filtered versions of which are plotted in Fig. 4. Specifically, the maps have been smoothed using a Gaussian beam of 1° *FWHM* to highlight any low-ℓ systematic effects, such as those due to intensity-to-polarization leakage. This first inspection indicates that these templates are not affected by any obvious low-ℓ systematic effects. More rigorous tests, however, are performed in Sect. 7.3 using intensity-to-polarization leakage corrected maps.

Then we have used the `SMICA` $\hat{Q}^{\text{lens}}$ and $\hat{U}^{\text{lens}}$ templates to make our secondary *B*-mode template, as described in Sect. 3.5. For illustration purposes, we have produced a *B*-mode template map by inverting $\hat{B}^{\text{lens}}_{\ell m}$ back to pixel-space through an inverse spherical harmonic transform. Although our *B*-mode template contains information in the multipole range $10 < \ell < 2000$, Fig. 5 shows two filtered versions of the *B*-mode map to highlight different ranges of angular scale. The high-resolution map (which is simply slightly smoothed using a Gaussian beam of 10′ *FWHM*) should show any important foreground contamination at small angular scales, whereas the low-resolution one (which is smoothed using a 1° Gaussian beam and downgraded to $N_{\text{side}} = 256$ `HEALPix` resolution) should reveal any large angular scale systematic effects. No evident systematic effects are

observed in the maps plotted in Fig. 5. In Sect. 7, we further assess the template robustness against various systematic effects by means of a series of tests at the power spectrum level.
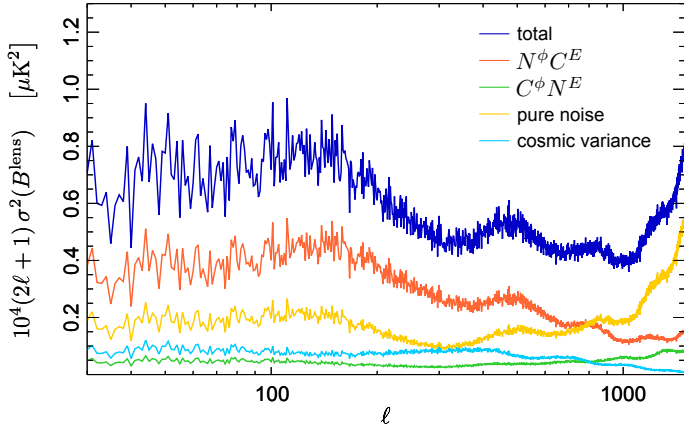
6.2. Variance contributions

In this section, we describe and quantify the various contributions that enter the template map variance. In particular, ranking the sources of variance helps us in quantifying the template variance dependence in the choice of the lensing potential estimates discussed in Sect. 3.3. This also anticipates the discussion that we develop in Sect. 8 on the utility of the *Planck* template for other experiments that are attempting to measure the lensing *B*-modes, compared to the use of a template that combines the *Planck* lens reconstruction and the experiment's *E*-mode measurement.

Using the auto-power spectrum estimate $\hat{C}^{B^{\text{lens}}}_{\ell}$ computed on the apodized masked template, the template variance is

$$\sigma^2\left(B^{\text{lens}}\right) = \frac{1}{f^{\text{eff}}_{\text{sky}}(2\ell+1)} \hat{C}^{B^{\text{lens}}}_{\ell}, \tag{16}$$

where $f^{\text{eff}}_{\text{sky}}$ is the effective sky fraction that is preserved by the apodized B70 mask. This receives three main contributions: cosmic variance of both the CMB *E*-modes and the lenses; instrumental noise; and lens reconstruction noise. For the sake of completeness, other sub-dominant contributions could include

Fig. 6. Template map variance budget. The total variance of the template, plotted in dark blue, is split into the contribution of the lens reconstruction noise (orange) and E-mode noise (green) cross-terms; and the pure noise (yellow) and cosmic variance (light blue) terms defined in Sect. 6.2.

foreground residuals, higher-order terms and secondary contractions of the CMB trispectrum (such as the so-called $N^{(1)}$ bias of the lens reconstruction). Within this model, $C_\ell^{B^{\text{lens}}}$ can be analytically calculated using

$$C_\ell^{\hat{B}^{\text{lens}}} = \mathcal{B}_\ell^{-2} \sum_{L\ell'} (f_L^\phi)^2 (C_L^{\phi,\text{fid}} + N_L^\phi) (f_{\ell'}^E B_{\ell'})^2 (C_{\ell'}^{E,\text{fid}} + N_{\ell'}^E) \, _2F_{\ell L\ell'}, \tag{17}$$

where the notation is the same as in Eqs. (10) and (12). Although the variance is evaluated using the template power spectrum estimate, Eq. (17) provides us with a useful tool for isolating the relative contributions to the total variance of the template. It can be decomposed into four terms: the "cosmic variance" contribution, which arises from the product of the ϕ and E power spectra; the "pure noise" contribution, which involves the product of both noise spectra; and two cross-terms, namely the "ϕ-noise primed" contribution $N_L^\phi C_\ell^E$ and the "E-noise primed" contribution $C_L^\phi N_\ell^E$. In Fig. 6, we plot the different contributions to the total variance of the template. The template variance is dominated by the ϕ-noise primed cross-term, which contributes an amount of about 60% to the total variance. To further quantify the template variance dependence on the ϕ estimate, we have rescaled N_L^ϕ by a factor of 0.75 in Eq. (17), which represents a simple way to emulate the precision gain that could be obtained by including the polarization-based ϕ reconstruction and a more precise ϕ estimate at high multipoles (e.g. using the CIB as a mass tracer). This has resulted in a 20% reduction of the template variance. This, in turn, has been propagated to the variance of the BB^{lens} measurement using Eq. (15), and has induced a 12% improvement of the signal detection significance, in agreement with the independent analysis reported in Planck Collaboration XV (2016) and discussed in Sect. 7.4.

The E-mode noise power spectrum, which contributes mainly through the pure noise term, provides less than 35% of the variance up to $\ell = 800$. As a consequence, very little leverage is left for other experiments to improve on the template uncertainties by producing a new template that combines each experiment's E-mode measurement with the *Planck* lensing potential reconstruction. In Sect. 8, we see that the *Planck* template offers other experiments a useful tool for measuring the lensing B-modes.

7. Robustness tests of our template

We now perform a series of consistency tests to characterize the B-mode template described in Sect. 6, with a view to using it for measuring the lensing C_ℓ^B in cross-correlation with observed polarization maps. In Sect. 7.2, we assess the template robustness against foreground residuals, first in varying the morphology and level of conservatism of the mask, and then in using foreground-cleaned CMB maps obtained with four independent component-separation algorithms. In Sect. 7.3, we use the *Planck* polarization maps in individual frequency channels to assess the stability of the lensing C_ℓ^B estimates with respect to the observed map to which our template is correlated. In Sect. 7.4, we discuss the consistency of the baseline lensing B-mode power spectrum presented here with the independent determination in Planck Collaboration XV (2016), which used various mass tracers. Finally, in Sect. 7.5, the *Planck* lensing C_ℓ^B measurements obtained using the B-mode template is compared to external measurements.

7.1. Template tests using B-mode band-power estimates

With the aim of testing the B-mode template, we have followed the template-based cross-correlation power spectrum approach that we developed to validate our pipeline via simulations, as described in Sect. 5.1. The tests that have been performed there also allow for an end-to-end assessment of the entire pipeline, whose main specifications are recalled below. Using FPP8 MC simulations for the SMICA method, together with the B70 template mask, we found that: (i) unbiased lensing B-mode band-power estimates are obtained by cross-correlating the B-mode template estimate with the input B-mode map; and (ii) the semi-analytical Gaussian variance given in Eq. (15) provides a good approximation for the uncertainties. To test the consistency of the band-power estimates with theoretical expectations, we fitted an amplitude with respect to the fiducial C_ℓ^B band-powers, and found an average value of 0.989 ± 0.008, which indicates that the lensing B-mode signal is accurately retrieved.

Here, we have used the B-mode template presented in Sect. 6 in cross-correlation with the SMICA foreground-cleaned polarization maps, and have applied the B70 template mask to obtain a baseline lensing B-mode band-power estimate, which is compared below to various other estimates. We further check the consistency between the baseline and alternative estimates by comparing the measured amplitude difference to the expected variance of the difference in Monte-Carlo simulations.

7.2. Robustness against foreground residuals

The robustness of the baseline measurements against the impact of foregrounds is assessed by comparison with alternative estimates that have different residuals. A first sequence of alternative estimates have been obtained by employing masks of various levels of conservatism with respect to the Galactic and extra-galactic foregrounds in temperature and polarization. These are detailed in Sects. 7.2.1 to 7.2.3. The corresponding fitted $A_{B\text{lens}}$ amplitudes and differences from the B70 estimate are listed in Table 2. Secondly, we consider measurements obtained with foreground-cleaned maps using different component-separation methods and give the resulting amplitudes in Sect. 7.2.3.

Table 2. Band-power amplitudes for various analysis masks, which are listed in the first column.

Mask label	$f_{\text{sky}}^{\text{eff}}$	$A_{B\text{lens}}$	S/N	$\Delta \pm \sigma_\Delta$
B70	0.65	0.96 ± 0.08	11.9	n. a.
B60	0.54	0.98 ± 0.09	11.1	-0.02 ± 0.04
B70p	0.64	0.94 ± 0.08	11.3	0.02 ± 0.02
B70s	0.61	0.97 ± 0.08	11.8	-0.01 ± 0.04
B80	0.69	1.00 ± 0.08	12.8	-0.04 ± 0.03

Notes. The column labelled $f_{\text{sky}}^{\text{eff}}$ give the effective sky fraction preserved by the apodized masks. The measured band-power amplitudes are given in the column labelled $A_{B\text{lens}}$, and the corresponding lensing *B*-mode detection significance levels in the column labelled S/N. The difference between the test amplitudes and the baseline B70 amplitude is given, where applicable, as Δ, together with the expected difference σ_Δ estimated using Monte-Carlo simulations.

7.2.1. Galactic contamination tests

We test for residual foreground contamination around the Galactic plane by comparing the B70 lensing *B*-mode estimate to estimates using the more conservative B60 mask and the more aggressive B80 mask, discussed in Sect. 4. We recall that B80 includes a Galactic mask that preserves 80% of the sky; this Galactic mask has been extended by 3° beyond its boundaries for constructing B70, while B60 includes a larger diffuse Galactic mask that retains about 60% of the sky. We have employed the apodized version of the masks using cosine tapers, as described in Sect. 4. For B80, however, we have used slightly larger apodization widths, namely 3° for the Galactic mask (instead of 2°) and 1° for the extended compact object mask (instead of 30′).

The lensing C_ℓ^B band-power estimates using the B60, B70, and B80 masks are shown in Fig. 7, and the fitted amplitudes are listed in Table 2. Both the B60 and B80 estimates are consistent with the B70 estimate. In particular, the agreement between the B60 and B70 lensing *B*-mode estimates indicates that any impact of Galactic foreground residuals lies well below the uncertainties. The consistency between the B70 and B80 estimates further indicates that: (i) an 80% Galactic cut suffices to avoid any Galactic foreground residuals in the SMICA map; and (ii) any leakage near the border of the mask (treated by inpainting) has negligible impact.

7.2.2. Extragalactic object contamination tests

For extracting the lensing potential ϕ map estimate that is used for the *B*-mode template synthesis, we have employed the L80 lensing mask described in Sect. 4.2. This cuts out any point sources included in the intersection of the conservative compact object mask described in Sect. 4.1 and the SMICA confidence mask. Here we test the stability of the *B*-mode estimate through the use of a more conservative point source mask that involves the union of these two masks. Namely, we have produced an alternative estimate that relies on a ϕ reconstruction using the L80s lensing mask, which includes the union of the compact object and the SMICA masks (see Sect. 4.2). In L80s, the sky area that is removed due to the expected point source contamination is increased by a factor of 2.3 compared to the L80 case. The extended object mask is also slightly enlarged by 25% due to areas of radius between 30′ and 120′ located at intermediate Galactic latitudes that are present in the SMICA confidence
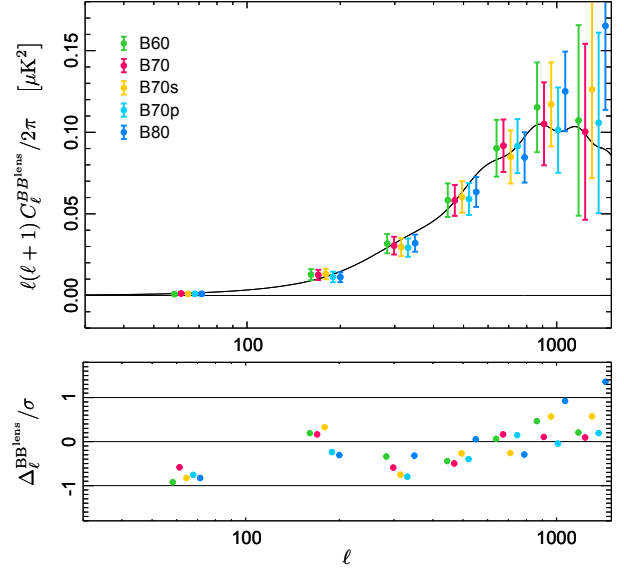
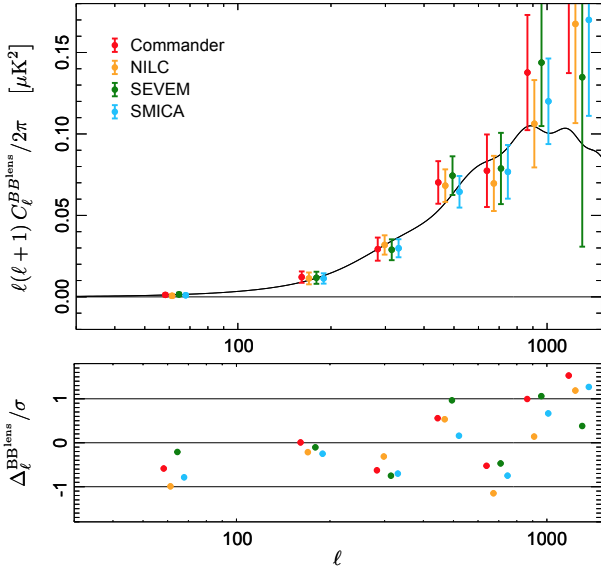**Fig. 7.** Cross-correlation of our *B*-mode template with the SMICA polarization map using masks of different levels of conservatism. The data points show the lensing C_ℓ^B band-powers estimated using masks that preserve a sky fraction of about 60% (labelled B60), 70% ("B70"), and 80% ("B80"), and that are targeted to the foreground emission in temperature (see Sect. 7.2.1); as well as using the 68% "B70s" mask, which allows for a more conservative masking of the extragalactic objects (see Sect. 7.2.2), and the 68% polarization-targeted "B70p" mask (see Sect. 7.2.3). The residuals with respect to the model in units of the 1σ band-power uncertainties are shown in *the lower panel*. The good agreement of all cases within error-bars provides a robustness test against foregrounds, as discussed in Sect. 7.2.

mask. The *B*-mode band-powers have then been estimated using the corresponding B70s mask for the template (which removes 1% more sky fraction than the baseline B70 mask, including about a hundred additional extragalactic objects). The B70s band-power estimate, which is plotted in Fig. 7, is consistent with the baseline B70 estimate within uncertainties. The fitted amplitude difference from the B70 estimate, which is given in Table 2, is well within the expected difference estimated from simulations. This validates the choices we made to include the expected point sources to our baseline mask, and indicates that our analysis is free from any sizeable bias due to extragalactic objects.

7.2.3. Polarized foreground emission tests

We test for the impact of polarized foreground residuals by comparing the B70 estimate to an estimate using the B70p mask targeted at the SMICA polarization maps, as discussed in Sect. 4.3. The B70p mask discards a sky fraction 2.5% larger than B70, mainly because of extended areas at medium latitude that may be contaminated by polarized foreground residuals. The lensing *B*-mode band-power estimates using the B70 and B70p masks are plotted in Fig. 7 and the corresponding amplitude fits are given in Table 2. The B70p estimate well agrees with the B70 estimate. We therefore expect no significant bias related to polarized foreground residuals.

From the tests performed so far, the results of which are gathered in Table 2, we have found all the band-power estimates, from the most conservative $f_{\text{sky}} = 0.58$ to the most optimistic $f_{\text{sky}} = 0.77$ analysis and whatever the morphology of the mask, in good agreement with the baseline estimate. This provides an

Fig. 8. Consistency of our results using the four *Planck* component-separation algorithms. The data points shown in *the upper panel* represent the lensing *B*-mode band-power measurements obtained by cross-correlating the lensing *B*-mode template estimates using the `Commander` (red), `NILC` (orange), `SEVEM` (forest green), and `SMICA` (blue) cleaned polarization map with the corresponding *B*-mode map. The residuals with respect to the model in units of the 1σ band-power uncertainties are shown in *the lower panel*. The consistency of the four estimates strongly indicates the robustness of our baseline template against polarized foreground residuals, as discussed in Sect. 7.2.3.

Fig. 9. Stability to the change in the observed polarization map. Data points shown in the *upper panel* are the $BB^{\rm lens}$ band-powers obtained from the cross-correlation of our `SMICA` *B*-mode template with the `SMICA` polarization map (red), and with single frequency polarization maps at 100 GHz (yellow), 143 GHz (green), and 217 GHz (blue), which were corrected for foreground and intensity-to-polarization leakage. Residuals with respect to the model in units of the 1σ band-power uncertainties are shown in *the lower panel*.

indication that (i) the *B*-mode template is robust against any foreground contamination or any impact of the sky-cut; and (ii) it allows us to obtain reliable lensing C_ℓ^B measurements for up to 70% of the sky.

We further test our template robustness against foreground residuals by comparing results using the four *Planck* component-separation methods, as described in Planck Collaboration IX (2016). We have focused on the polarized foreground residuals; we have used different foreground-cleaned Stokes parameter maps, but the same temperature map: specifically, the lensing *B*-mode templates have been synthesized from the foreground-cleaned Stokes *Q* and *U* maps using different codes and a fixed lensing potential extraction obtained from the `SMICA` temperature map. For this specific test, we have produced a common mask that combines the B80 mask and the union of the confidence masks provided by each of the component-separation methods described in Planck Collaboration IX (2016). The common mask retains a sky fraction of 75% for analysis, and its apodized version preserves an effective sky fraction of 62%. Figure 8 shows the resulting lensing *B*-mode power spectra, obtained through cross-correlation of the lensing *B*-mode templates with the input Stokes *Q* and *U* maps from the corresponding component-separation method.
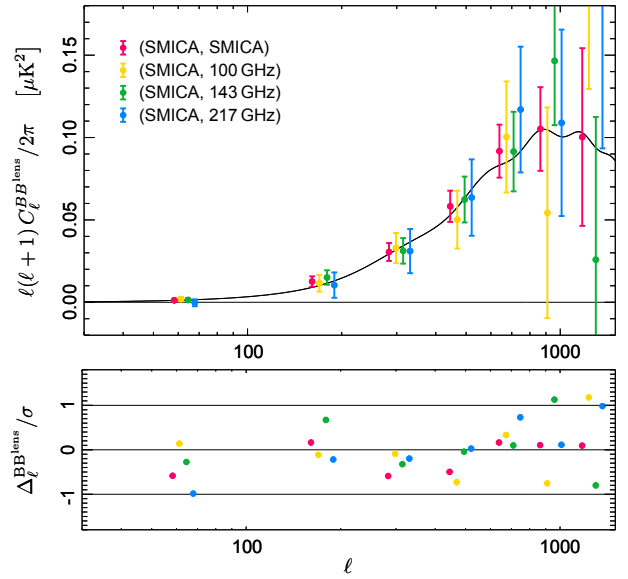
The four Stokes *Q* and *U* foreground-cleaned solutions lead to consistent lensing *B*-mode power spectrum measurements (within 1σ) over the entire multipole range probed. We measure fits to the amplitude with respect to the fiducial model of:

$A_{B\rm lens} = 1.01 \pm 0.11$ (`Commander`);

$A_{B\rm lens} = 0.97 \pm 0.09$ (`NILC`);

$A_{B\rm lens} = 1.00 \pm 0.10$ (`SEVEM`);

$A_{B\rm lens} = 0.97 \pm 0.08$ (`SMICA`).

These correspond to 9.5σ, 11.3σ, 9.7σ, and 11.8σ detections of the lensing *B*-modes, respectively. The consistency of the lensing C_ℓ^B measurements based on four CMB solutions with different foreground residuals indicates the immunity of our baseline lensing *B*-mode template to polarized foreground emission.

7.3. Stability with respect to the observed polarization

So far, we have considered the cross-correlation of the *B*-mode template synthesized from the Stokes *I*, *Q*, and *U* foreground-cleaned maps, with the same *Q*, *U* maps. We now test the cross-correlation of our baseline template with other CMB foreground-cleaned polarization maps. In particular, we have used foreground and intensity-to-polarization leakage-corrected *Planck* channel maps at 100, 143, and 217 GHz, which also serve to test the robustness of our template against low-ℓ systematic effects. These single channel maps rely on the pre-launch ground-based measurements of the detector bandpasses to correct for the intensity-to-polarization leakage due to bandpass mismatch between the detectors within a frequency channel, as described in Planck Collaboration VIII (2016). The polarized emission of the Galactic dust has been corrected for by using the 353-GHz map as a dust template.

In Fig. 9, we compare the baseline $BB^{\rm lens}$ band-powers from the B70 `SMICA` analysis to the band-powers obtained by correlating our `SMICA` *B*-mode template with the *B*-mode maps at 100, 143, and 217 GHz built out of the corresponding single channel foreground-cleaned polarization maps and using the same B70 mask. The band-power estimates are in good agreement with each other within uncertainties, indicating the robustness of our template against polarization systematic effects (that mainly affect the low multipoles). We find that our lensing *B*-mode template provides stable measurements of the CMB

lensing *B*-modes independent of the choice of the polarization maps with which it is correlated.

7.4. Consistency with previous Planck results

First of all, we have checked that the baseline lensing *B*-mode power spectrum presented here is consistent with the independent determination of Planck Collaboration XV (2016) over the $100 < \ell < 2000$ multipole range, which provides us with further validation of our methodology choices[7].

In Planck Collaboration XV (2016), lensing-induced *B*-mode power spectrum measurements have been obtained using various mass tracers: lensing potential reconstructions using either both temperature and polarization data or temperature data only; and CIB fluctuations measured by *Planck* in the 545-GHz channel. The latter have relied on a model of the CIB emission for calculating its cross-correlation with the lensing potential. All cases have been consistent with theoretical expectations and in good agreement with each other, which validates the stability of the measurement with respect to the mass tracer choice. The additional information brought by the polarization-based ϕ estimates yields a 10% improvement of the lensing B-mode detection significance compared to the case using the temperature-based ϕ estimate, whereas the use of the CIB fluctuations as a mass tracer lowers the detection significance by roughly the same amount. Thus, including the polarization information for reconstructing ϕ or using the CIB as a mass tracer would not have substantially improved the uncertainties of the *B*-mode template that we have produced.

7.5. Consistency with external results

Our BB^{lens} band-power estimates are a measurement of the lensing *B*-mode power spectrum that we now compare to measurements reported by other experiments.

As stated in Sect. 1, the available *B*-mode measurements come in two flavours: the *BB* power spectrum of the observed polarization maps measures the total *B*-mode signal; whereas the BB^{lens} power spectrum between a template and the observed polarization maps probes the secondary contribution only.

In Fig. 10, we gather the composite C_ℓ^B measurements obtained by BICEP2/Keck Array, POLARBEAR, SPTpol, and the *Planck* mission, which represents the landscape of current CMB *B*-mode band-power estimates. The *BB* power spectrum measurements of BICEP2/Keck Array[8], POLARBEAR (The Polarbear Collaboration 2014) and SPTpol (Keisler et al. 2015) are collected by the brace labelled *BB* in Fig. 10. For BICEP2/Keck Array, we plot the *B*-mode band-powers in the multipole range $20 < \ell < 335$, obtained from the combination of the BICEP2 and Keck Array maps reported in BICEP2 and Keck Array Collaborations (2015a) and corrected for polarized dust emission using *Planck* data, as described in BICEP2/Keck Array

---
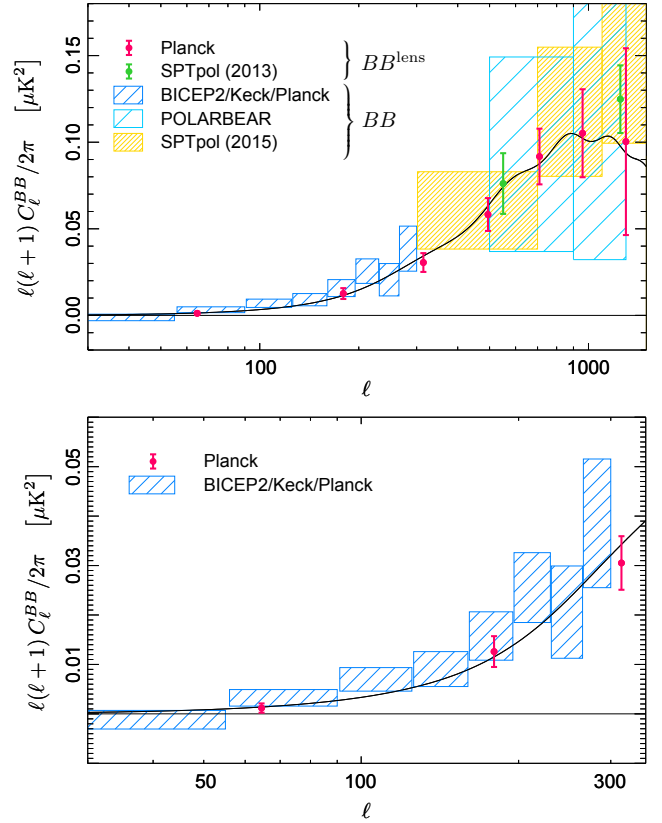
Fig. 10. Consistency with external *B*-mode power spectrum measurements on the full multipole range (*top*) and at $\ell < 350$ (*bottom*). We compare our baseline BB^{lens} estimate (red points) to the SPTpol template-based results (green points; Hanson et al. 2013); and to the *BB* power spectrum measurements from BICEP2/Keck Array (blue boxes; BICEP2 and Keck Array Collaborations 2015a), POLARBEAR (light blue boxes; The Polarbear Collaboration 2014), and SPTpol (yellow boxes; Keisler et al. 2015), as discussed in Sect. 7.5. The black line shows the theoretical lensing *B*-mode power spectrum for the base ΛCDM best-fit *Planck* model (with $r = 0$).

and Planck Collaborations (2015, which is referred to as BKP hereafter). The BB^{lens} measurements of SPTpol (Hanson et al. 2013) and *Planck* (this analysis) are gathered by the brace labelled BB^{lens}. For *Planck* BB^{lens} band-powers, we select the B70 analysis whose robustness has been assessed in Sect. 7.2. The 4.2σ lensing *B*-mode detection reported by the POLARBEAR team (Ade et al. 2014b) and the 3.2σ detection obtained by ACTpol (van Engelen et al. 2015) are not shown in Fig. 10 for clarity.

Our *Planck*-derived BB^{lens} band-powers are in good agreement with other *B*-mode measurements, using both the *BB* or the BB^{lens} power spectrum methods. *Planck* provides the most precise measurement of the lensing-induced *B*-mode power spectrum to date (as assessed in Planck Collaboration XV 2016). Covering a wide multipole range $10 < \ell < 2000$, our band-powers consists of lensing C_ℓ^B measurements at a significance level as high as 12σ. It is also worth focusing on the low-ℓ range. The C_ℓ^B measurements are expanded at $\ell > 350$ in the lower panel of Fig. 10, which illustrates the lensing *B*-mode template utility for the primordial-to-secondary *B*-mode discrimination. Using *Planck* data alone, which combines wide sky coverage, necessary to probe low multipoles, and a good angular resolution, needed for the lensing potential extraction, the

lensing *B*-mode template enables us to extend the measure of the lensing-induced C_ℓ^B into the low multipole range.

8. Implications for current and future *B*-mode experiments

Here, we address the implications of the template for experiments targeting primordial *B*-modes. A full joint analysis using external data is beyond the scope of this paper. However, as examples we discuss two different aspects. First, we address to what extent the template can help experiments in measuring the lensing *B*-mode power spectrum, in particular over the largest accessible angular scales. Secondly, we forecast the improvement of the lensing amplitude measurement when using the *Planck* lensing *B*-mode template, and we discuss whether this improvement can translate into a better sensitivity to the tensor-to-scalar ratio.

8.1. Measurement of the lensing B-mode power spectrum

Since the *Planck* lensing *B*-mode template covers almost the entire sky, polarization measurements from any *B*-mode experiment can be cross-correlated with the template. This ensures a valuable lensing *B*-mode power spectrum measurement, including the intermediate angular scales, where the lensing signal is of the same order of magnitude or sub-dominant with respect to the polarized foreground emission (see Planck Collaboration Int. XXX 2016, hereafter referred to as PIP-XXX).

For current ground-based experiments, the cross-correlation with the *Planck* template is a promising method for measuring the lensing *B*-mode signal at the largest accessible angular scales. In general, it leads to better results than a cross-correlation with a lensing *B*-mode template built out of the *Planck* lensing potential and each experiment's *E*-mode map. This can be understood from two different considerations. On the one hand, a study of the lensing *B*-mode signal kernel (as in Fabbian & Stompor 2013; Simard et al. 2015) reveals that most of the signal at low and intermediate angular scales comes from products of the lensing potential power at low multipoles and the *E*-mode power at higher multipoles. For example, at $\ell = 100$ (200), 80% (90%) of the lensing *B*-mode power arises from *E*-mode power at $\ell > 335$. For degree-scale experiments, such as BICEP, it would be of little value to use its own *E*-mode data to generate a new lensing *B*-mode template. On the other hand, in Sect. 6.2, we have found the *B*-mode template variance to be dominated by the contribution arising from the noise power spectrum of the reconstructed lensing potential N_L^ϕ, even for the *Planck* *E*-mode noise. For high-resolution experiments covering a small fraction of the sky, we do not expect that a better sensitivity in the *E*-modes compensates for the uncertainties linked to the small sky coverage. We have quantified this effect in using Eqs. (16) and (17) to forecast the template uncertainties, specifically for an ideal experiment providing noiseless *E*-mode measurements for multipoles from 30 to 2000 with a resolution of 1′ and a sky coverage of 1%. We find the uncertainties of the ideal experiment's *E*-mode-based template to be about five times larger than the *Planck* template uncertainties up to multipoles of 700 (and still 50% larger than those of the *Planck* template at $\ell = 2000$). We conclude that, for experiments covering less than a percent of the sky, such as SPTpol or POLARBEAR, the synthesis of a lensing *B*-mode template that combines the experiment's *E*-mode data with *Planck* ϕ estimate would degrade

the signal-to-noise for measuring the lensing *B*-mode power spectrum.

8.1.1. Uncertainty forecasting method

We forecast the uncertainties of the lensing *B*-mode power spectrum measurement that current experiments can obtain from cross-correlating their *B*-mode signal with the *Planck* lensing *B*-mode template. As in Sect. 7.5, we consider the BICEP2/Keck Array, POLARBEAR, and SPTpol examples. Error bars are evaluated using Eq. (15). They include lensed cosmic variance from the best-fit ΛCDM model and the statistical error from the template (the template auto-power spectrum $\hat{C}_\ell^{B\mathrm{lens}}$ factor) and from the experiment (the experiment auto-spectrum $(C_\ell^B + N_\ell^B)$ factor). To estimate the template variance within the experiment's field, $\hat{C}_\ell^{B\mathrm{lens}}$ is analytically calculated using the lensing potential and *E*-mode noise power spectra, rescaled to the noise spatial inhomogeneity within the experiment's field. This rescaling relies on the SMICA hit count map. We use a simplified model for the *BB* auto-spectrum of the experiment that includes the lensed CMB *B*-modes, polarized dust, white noise, and Gaussian beam. The specific model and analysis choices are detailed below.

The polarized dust emission has been parametrized by a single free amplitude in power, A_{dust}, which is defined at the reference frequency of 353 GHz and at a multipole of $\ell = 80$. Following PIP-XXX, the dust power spectrum has been modelled as the power law $C_\ell^{\mathrm{dust}} \propto \ell^{-2.42}$, with a spatially uniform frequency scaling according to a modified black-body law, assuming a fixed dust temperature $T_{\mathrm{d}} = 19.6$ K and spectral index $\beta_{\mathrm{d}} = 1.6$. For the BICEP2/Keck Array combination, we have fixed the dust amplitude to the best-fit value obtained in the joint BICEP2/Keck Array and *Planck* analysis described in BKP, namely $A_{\mathrm{dust}} = 3 \mu\mathrm{K}^2$. In PIP-XXX, individual dust amplitudes have been fitted for a series of sky patches, and their scaling with the mean 353-GHz dust intensity was described using an empirical relation. However, there was a warning about the difficulty in deriving precise dust amplitude estimates from this empirical law. From Fig. 7 of PIP-XXX, we can see that, at the low dust intensity values expected in the SPTpol and POLARBEAR fields, the amplitudes range from 0.1 to $10 \mu\mathrm{K}^2$. For simplicity, we have assumed the level of dust emission in the POLARBEAR and SPTpol fields to be the same as in the BICEP2 field, and so have used the value $A_{\mathrm{dust}} = 3 \mu\mathrm{K}^2$. We checked that assuming the more pessimistic $A_{\mathrm{dust}} = 10 \mu\mathrm{K}^2$ leads to a minor increase in the forecast-ed BB^{lens} band-power uncertainties.

The BICEP2/Keck Array combination has been modelled as reaching a noise level of $3.4 \mu\mathrm{K}$ arcmin over $400 \deg^2$, and as having a Gaussian beam of 31′ *FWHM* for both BICEP2 and Keck Array experiments (BICEP2 and Keck Array Collaborations 2015b,a). POLARBEAR has been modelled as reaching a depth of $8 \mu\mathrm{K}$ arcmin over an effective sky area of $25 \deg^2$ ($f_{\mathrm{sky}} = 0.06\%$) with 3′.5 resolution at 150 GHz (The Polarbear Collaboration 2014). For SPTpol, we have modelled the noise spectrum from the characteristics reported in Hanson et al. (2013), by considering the combination of the 95-GHz observation (1′.83 resolution and $25 \mu\mathrm{K}$ arcmin noise level) and the 150-GHz observation (1′.06 resolution and $10 \mu\mathrm{K}$ arcmin noise level) over a sky area of $100 \deg^2$ ($f_{\mathrm{sky}} = 0.24\%$). We have used the same multipole binning as chosen by each experiment in existing publications, and have added a low-ℓ bin including multipoles up to the largest accessible angular scales defined by the
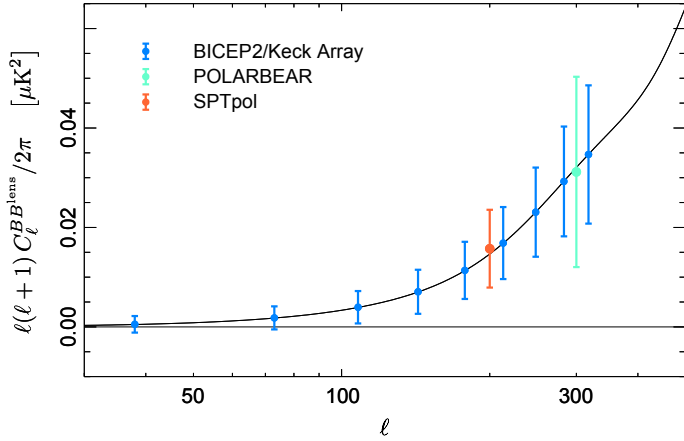
Fig. 11. Forecasts of lensing *B*-mode band-powers from cross-correlating the *Planck* lensing *B*-mode template with external data from *B*-mode targeted experiments. Blue circles show the BICEP2/Keck Array band-powers forecasts using the same multipole binning as that of BICEP2/Keck Array data points shown in Fig. 10. $BB^{\rm lens}$ band-power measurements can be extended to an additional $\ell = 100$–500 bin using POLARBEAR (turquoise) and to an additional $\ell = 100$–300 bin using the SPTpol (dark orange) in cross-correlation with the template.

experiment's sky coverage. For POLARBEAR and SPTpol, we have considered the $100 < \ell < 2000$ multipole range.

8.1.2. Lensing *B*-mode band-power forecasts

Figure 11 shows the forecast-ed $BB^{\rm lens}$ band-powers over multipoles up to 500, for which the *Planck* template is the most useful in helping other experiments to measure the lensing *B*-mode power spectrum. We find that the BICEP2/Keck Array could be used in combination with the *Planck* template to obtain $BB^{\rm lens}$ band-powers in the multipole range $\ell = 20$–335 measured at a significance level of about 6σ (sensitivity to $A_{B{\rm lens}}$ of 0.17). Therefore, our forecast-ed sensitivity to the lensing *B*-mode signal is comparable to that obtained in the BKP analysis, where a lensing amplitude of $A_{\rm lens} = 1.13 \pm 0.18$ has been measured. However, we show in Sect. 8.3 that we could improve the sensitivity to the lensing *B*-mode signal by adding the *B*-mode template to a BICEP2/Keck Array and *Planck* joint analysis. The *Planck* template could enables sub-degree angular scale experiments, such as BICEP2/Keck Array, to probe the ℓ-dependence of the lensing *B*-mode signal over their full multipole range, including multipoles at which the lensing-induced signal is subdominant compared to other sources of *B*-mode signal (such as polarized dust). Moreover, the cross-correlation with the template should allow experiments targeting higher multipoles (such as POLARBEAR or SPTpol) to measure the lensing *B*-mode signal at intermediate angular scales ($100 < \ell < 300$), extending their $BB^{\rm lens}$ estimates down to as low multipoles as their sky coverage would permit.

8.2. Direct delensing capabilities

"Delensing" consists of subtracting the lensing *B*-mode template from the *B*-mode map of an experiment in order to try to highlight the primordial *B*-modes. Because of the noise level of the template, poor efficiency is expected from a direct delensing approach (e.g. Marian & Bernstein 2007). We have quantified the expected impact on the tensor-to-scalar ratio uncertainty in calculating the improvement factor as defined in

Smith et al. (2009b) as

$$\alpha = \frac{C_\ell^{B,{\rm lens}} + N_\ell^B}{C_\ell^{B,{\rm res}} + N_\ell^B}. \tag{18}$$

Here $C_\ell^{B,{\rm lens}}$ and $C_\ell^{B,{\rm res}}$ are the lensing *B*-mode power spectrum, and its residual after subtraction of the template from the external data, while N_ℓ^B is the noise power spectrum of the experiment. We find a maximum improvement factor (corresponding to $N_\ell^B = 0$) of 5% at $\ell < 200$, reaching a maximum of 10% around $\ell = 300$, in agreement with the expectations derived in Smith et al. (2009b).

8.3. Improvement of the parameter accuracies

We now go beyond the lensing *B*-mode power spectrum measurement and quantify whether the use of the template as an additional data set (together with other *B*-mode data and the *Planck* dust template) can tighten cosmological parameter constraints, and in particular, the amplitude of the lensing potential power spectrum that scales the lensing-induced *B*-modes, $A_{\rm lens}$. We discuss whether more precise measurements of the lensing scaling translate into tightened constraints on the tensor-to-scalar ratio.

We derive forecasts for particular experiments by performing a Fisher analysis[9] (for a description of this method, see e.g. Tegmark et al. 1997). We consider a three-parameter model, $\{r, A_{\rm lens}, A_{\rm dust}\}$, consisting of the tensor-to-scalar ratio and the amplitudes of the lensing potential and polarized dust power spectra. We compare the parameter constraints obtained in two cases: (1) the data sets consist of $B^{\rm exp}$, the external data from the *B*-mode targeted experiment, and $\hat{B}^{\rm dust}$, the *Planck* *B*-mode data at 353 GHz, considered as a polarized dust template; and (2) the *Planck* lensing *B*-mode template, $\hat{B}^{\rm lens}$, is used in combination with the other two data sets. As examples of external experiments, we consider the BICEP2/Keck Array combination, hereafter referred to as BK, described in BICEP2 and Keck Array Collaborations (2015a); and a wide sky coverage experiment, such as LiteBIRD (Matsumura et al. 2014). The rationale driving these choices is twofold. Because of the lensing *B*-mode template noise level in a 1% sky area and from the results obtained above, we do not expect the inclusion of the template to bring a large improvement of the sensitivity to r for BK. However, we will be able to validate our simple fiducial analysis by comparing "Case 1" to the floating lensing amplitude analysis described in BKP. By contrast, a more substantial improvement is expected for a large sky coverage *B*-mode experiment such as LiteBIRD. For definiteness, we consider two different fiducial cosmologies in what follows, which consist of a $r = 0.05$ model and $r = 10^{-4}$ model.

8.3.1. Fisher analysis

We consider the Fisher information matrix of the form (see e.g. Tegmark et al. 1997)

$$F_{ij} = \sum_\ell \frac{1}{2}(2\ell + 1)f_{\rm sky}\,{\rm Tr}[{\rm CC}_{,i}{\rm CC}_{,j}] \tag{19}$$

---

[9] We note that in this approach, the parameter likelihood is assumed to be Gaussian close to its maximum, so that the parameter constraints can be derived by calculating the distribution Hessian taken at the fiducial values of the parameters. Owing to this assumption, parameter confidence contours are ellipses.

for a fiducial data covariance matrix C and its derivatives with respect to the parameters labelled by i and j. Given the data set $\{B_{\ell m}^{\text{exp}}, \hat{B}_{\ell m}^{\text{dust}}, \hat{B}_{\ell m}^{\text{lens}}\}$, we need to model the B-mode auto-power spectra for the external data, C_ℓ^{exp}, for the *Planck* 353-GHz map, C_ℓ^{353}, and for the *Planck* lensing B-mode template within the experiment's sky coverage, $C_\ell^{\hat{B}\text{lens}}$, as well as the corresponding cross-power spectra.

The fiducial model consists of an extension of the six-parameter ΛCDM model considered so far, including primordial gravitational waves (GW) of amplitude r, a freely floating amplitude of the lensing potential power spectrum, A_{lens}, and a free polarized dust amplitude in power A_{dust} (defined at the reference frequency of 353 GHz and at a multipole of $\ell = 80$). In this fiducial framework, the B-mode auto-power spectrum of the experiment under consideration is

$$C_\ell^{\text{exp}} = \frac{r}{r_{\text{fid}}} C_\ell^{\text{GW},r=r_{\text{fid}}} + A_{\text{lens}} C_\ell^{\text{lens}} + \alpha A_{\text{dust}} R(\nu, 353)^2 C_\ell^{\text{dust}} + N_\ell^{\text{exp}},$$
(20)

where $C_\ell^{\text{GW},r=r_{\text{fid}}}$ and C_ℓ^{lens} are the gravitational wave and lensing power spectra at the fiducial $r = r_{\text{fid}}$ and $A_{\text{lens}} = 1$ values. We have considered two different fiducial values for r, either $r_{\text{fid}} = 0.05$ or $r_{\text{fid}} = 10^{-4}$. The dust power spectrum, C_ℓ^{dust}, and its frequency scaling with the reference 353-GHz frequency, $R(\nu, 353)$ have been modelled as in Sect. 8.1, following PIP-XXX. In addition, for multi-band experiments with foreground-cleaning capabilities, the dust power spectrum has been assumed to be cleaned up to a residual level defined by the α factor ($\alpha = 1$ for a single frequency experiment). Finally, N_ℓ^{exp} is the B-mode noise power spectrum of each experiment.

The *Planck* 353-GHz B-mode auto-power spectrum in each experiment's sky coverage has been modelled as

$$C_\ell^{353} = A_{\text{dust}} C_\ell^{\text{dust}} + N_\ell^{353},$$
(21)

where the full-sky noise power spectrum at 353 GHz has been scaled to take the spatial inhomogeneity within the experimental field into account. We have neglected the sub-dominant CMB B-mode polarization signal.

Finally, the *Planck* lensing B-mode template auto-power spectrum within the experimental field has been analytically calculated using Eq. (17), in which the noise power spectra of the lensing potential N_L^ϕ and of the E-mode N_ℓ^E have been scaled to deal with the spatial inhomogeneity within the experimental field. The cross-correlation of the experiment's data with the 353-GHz dust template and lensing B-mode template are $(\alpha)^{0.5} A_{\text{dust}} R(\nu, 353) C_\ell^{\text{dust}}$ and C_ℓ^{lens}. Following the assumptions of the model, we have neglected the sub-dominant cross-correlation of the lensing B-mode and 353-GHz dust templates.

8.3.2. Examples of BK and LiteBIRD

For existing data, we have used a data-driven model. Both the BK and the *Planck* 353-GHz noise power spectra in the BK field have been extrapolated from the noise band-powers released along with the BKP likelihood[10]. For the future project LiteBIRD, we have modelled the noise power spectrum from the foreseen instrumental characteristics defined in Matsumura et al. (2014). Only the 100- and 140-GHz bands have been considered, the two lowest and two highest bands being discarded, assuming that they are used for foreground cleaning. Following

---

[10] http://bicepkeck.org/bkp2_2015_release.html

Table 3. Fisher analysis inferred parameter uncertainties for the BICEP2/Keck Array experiment and for the LiteBIRD project using the $r = 0.05$ and $r = 10^{-4}$ fiducial models.

Parameter	BICEP2/Keck[a]		LiteBIRD[b]	
	Case 1	Case 2	Case 1	Case 2
		$r = 0.05$		
Δr	0.031	0.030	0.0021	0.0018
ΔA_{lens} . . .	0.19	0.12	0.042	0.033
ΔA_{dust} . . .	0.7	0.6	0.05	0.05
		$r = 10^{-4}$		
Δr	0.025	0.024	0.00036	0.00035
ΔA_{lens} . . .	0.18	0.12	0.0205	0.0195
ΔA_{dust} . . .	0.6	0.6	0.05	0.04

Notes. [a] See BICEP2 and Keck Array Collaborations (2015a). [b] See Matsumura et al. (2014). Forecasts are given for two different data sets: "Case 1" consists of the experiment's data and the *Planck* 353-GHz map; and "Case 2" consists of the same two ingredients plus the *Planck* lensing B-mode template.

Matsumura et al. (2014), the 100-GHz band reaches a depth of $3.7\,\mu$K arcmin and a resolution defined by a Gaussian beam of 45′ *FWHM*, while the 140-GHz band has a noise level of $4.7\,\mu$K arcmin and 32′ *FWHM*. The polarized dust in each frequency band has been assumed to be cleaned over an effective sky area of 63% up to the same residual level as in the BK field. This corresponds to a mildly conservative (Dunkley et al. 2009) 17% residual level in the map domain (corresponding to $\alpha = 2.9\%$ in power) for the dust amplitude $A_{\text{dust}} = 104.5\,\mu$K^2, obtained in PIP-XXX via a power-law fit in the large retained science region "LR63".

With the fiducial model established and using the numerical analysis method described, we can infer the sensitivity to the parameters as $\Delta\theta_i = \sqrt{(F^{-1})_{ii}}$ for $\theta_i \in \{r, A_{\text{lens}}, A_{\text{dust}}\}$. The results for BK and LiteBIRD for the two fiducial values of r and in the two cases considered, depending on whether the lensing B-mode template is used or not, are presented in Table 3.

For the BK analysis in Case 1 (without the lensing template) and using the $r = 0.05$ fiducial model, we find $\Delta r = 0.031$, $\Delta A_{\text{lens}} = 0.186$ and $\Delta A_{\text{dust}} = 0.7$, in agreement with results reported in BKP: $r = 0.048^{+0.035}_{-0.032}$, $A_{\text{lens}} = 1.13 \pm 0.18$ (from the free lensing amplitude extended analysis) and $A_{\text{dust}} = 3.3^{+0.9}_{-0.8}$. This indicates that our fiducial Fisher analysis yields reliable parameter uncertainty estimates despite the underlying simplifying assumptions. The use of the lensing template translates into a 5% improvement of the r constraint, whereas the constraint on A_{lens} is tightened by 36%. Similar results are found using the more pessimistic $r = 10^{-4}$ fiducial model; Case 2 yields a 5% improvement of the constraint on r and a 35% improvement of the constraint on A_{lens}, compared to Case 1. Over the multipole range covered by BK, A_{lens} is weakly correlated with both r and A_{dust}, as was noted in the BKP paper, so that the improvement in the A_{lens} constraint translates into modest improvement of the r or A_{dust} constraints. This is verified in Fig. 12, where the two-dimensional contours at 68% and 95% are shown in the A_{lens}–r and A_{lens}–A_{dust} planes. However, Fig. 12 also shows that the A_{lens}–r correlation is further reduced when the lensing B-mode template is used, leading to more robust constraints.

For large angular scale experiments whose multipole coverage is limited to $\ell \lesssim 200$, such as LiteBIRD, the implication of
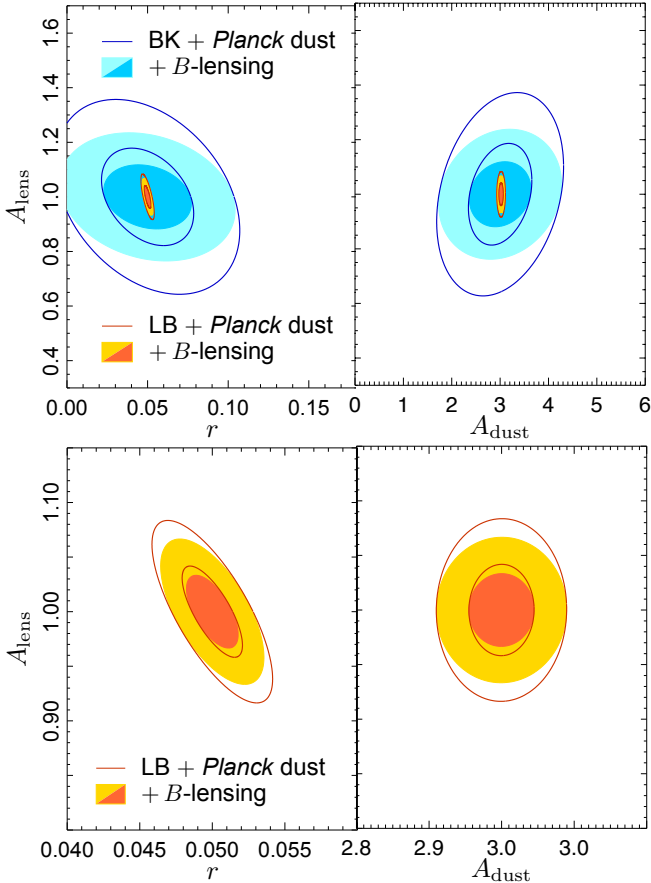
Fig. 12. Constraints on the tensor-to-scalar ratio *r* and the amplitude of the polarized dust power $A_{\rm dust}$ within a model with free lensing potential amplitude $A_{\rm lens}$. The two-dimensional likelihood contours at 68% and 95% are forecasted for BICEP2/Keck Array (BK, shades of blue) and for LiteBIRD (LB, shades of red), in combination with the *Planck* 353-GHz dust template only (line contours) and the *Planck* dust and lensing *B*-mode templates (shaded contours). The *lower panels* show a zoom-in on the LiteBIRD contours.

the template slightly differs. For the $r = 10^{-4}$ fiducial model, the secondary *B*-modes, which fully dominate over the primary *B*-modes, are precisely measured even without the help of the template. In the $r = 0.05$ fiducial model, however, the lack of measurement over a lensing *B*-mode dominated multipole range increases the parameter degeneracy, in particular between $A_{\rm lens}$ and *r*, as seen in Fig. 12. As a result, the 20% improvement on the $A_{\rm lens}$ uncertainties, which arises from using the *Planck* lensing *B*-mode template, translates into a 15% improvement on the *r* uncertainties.

9. Conclusions

We have produced a nearly all-sky template of the CMB secondary *B*-modes using the *Planck* full-mission foreground-cleaned CMB temperature and Stokes parameter maps. For this purpose, we have developed a dedicated pipeline that has been verified via specific simulations. We show that the constructed template includes the lensing *B*-mode contribution at all angular scales covered by *Planck* and shows no contamination from primordial *B*-modes. This template has been used to compute the CMB lensing *B*-mode power spectrum by cross-correlating it with the total foreground-cleaned *Planck* polarization *B*-mode maps (via the publicly available *Q* and

U maps). We find that the resulting CMB lensing *B*-mode power spectrum is insensitive to foreground contamination and independent of the choice of the foreground-cleaned *Planck* polarization *B*-mode map used for the cross-correlation analysis. Furthermore, we find that the results are in good agreement with the expected CMB lensing *B*-mode power spectrum computed using the baseline *Planck* 2015 best-fitting Λ-CDM model. We obtain a 12σ detection of the lensing *B*-modes, in agreement with the results in the companion Planck Collaboration XV (2016) paper.

Planck provides a unique nearly all-sky lensing *B*-mode template, containing all the lens-induced information from intermediate to large angular scales. This template, which is included as part of the *Planck* 2015 data release, will be a useful tool for current and future ground-based experiments targeting the measurement of the primordial CMB *B*-mode power spectrum. Indeed, this template can be used to obtain a reliable measurement of the lensing *B*-mode power spectrum with future experiments or to improve the precision with which they can detect the lensing *B*-modes in their own data, by tightening the constraints on the lensing amplitude. This, in turn, can help in the more challenging endeavour of constraining the tensor-to-scalar ratio.

References

Abrial, P., Moudden, Y., Starck, J., et al. 2007, J. Fourier Anal. Applic., 13, 729
Ade, P. A. R., Aikin, R. W., Barkats, D., et al. 2014a, Phys. Rev. Lett., 112, 241101
Ade, P. A. R., Akiba, Y., Anthony, A. E., et al. 2014b, Phys. Rev. Lett., 113, 021301
Benoit-Lévy, A., Déchelette, T., Benabed, K., et al. 2013, A&A, 555, A37
Bernardeau, F. 1997, A&A, 324, 15
BICEP2 and Keck Array Collaborations. 2015a, ApJ, 811, 126
BICEP2 and Keck Array Collaborations. 2015b, ApJ, 806, 206
BICEP2/Keck Array and Planck Collaborations. 2015, Phys. Rev. Lett., 114, 101301
Blanchard, A., & Schneider, J. 1987, A&A, 184, 1
Delabrouille, J., Cardoso, J.-F., & Patanchon, G. 2003, MNRAS, 346, 1089
Dunkley, J., Amblard, A., Baccigalupi, C., et al. 2009, in AIP Conf. Ser. 1141, eds. S. Dodelson, D. Baumann, A. Cooray, et al., 222
Fabbian, G., & Stompor, R. 2013, A&A, 556, A109
Górski, K. M., Hivon, E., Banday, A. J., et al. 2005, ApJ, 622, 759
Grishchuk, L. P. 1975, Sov. J. Exp. Theor. Phys., 40, 409
Guth, A. H. 1981, Phys. Rev. D, 23, 347
Hanson, D., Hoover, S., Crites, A., et al. 2013, Phys. Rev. Lett., 111, 141301
Hu, W. 2000, Phys. Rev. D, 62, 043007
Hu, W. 2001a, Phys. Rev. D, 64, 083005
Hu, W. 2001b, ApJ, 557, L79
Hu, W., & Okamoto, T. 2002, ApJ, 574, 566
Kamionkowski, M., Kosowsky, A., & Stebbins, A. 1997, Phys. Rev. Lett., 78, 2058
Keisler, R., Hoover, S., Harrington, N., et al. 2015, ApJ, 807, 151
Knox, L. 1995, Phys. Rev. D, 52, 4307
Lewis, A., & Challinor, A. 2006, Phys. Rep., 429, 1
Linde, A. D. 1982, Phys. Lett. B, 108, 389
Marian, L., & Bernstein, G. M. 2007, Phys. Rev. D, 76, 123009
Matsumura, T., Akiba, Y., Borrill, J., et al. 2014, J. Low Temp. Phys., 176, 733
Namikawa, T., & Nagata, R. 2014, J. Cosmol. Astropart. Phys., 9, 009
Okamoto, T., & Hu, W. 2003, Phys. Rev. D, 67, 083002

Perotto, L., Bobin, J., Plaszczynski, S., Starck, J.-L., & Lavabre, A. 2010, A&A, 519, A4

Planck Collaboration VII. 2011, A&A, 536, A7

Planck Collaboration XVIII. 2011, A&A, 536, A18

Planck Collaboration XII. 2014, A&A, 571, A12

Planck Collaboration XIII. 2014, A&A, 571, A13

Planck Collaboration XVI. 2014, A&A, 571, A16

Planck Collaboration XVII. 2014, A&A, 571, A17

Planck Collaboration XVIII. 2014, A&A, 571, A18

Planck Collaboration XXVIII. 2014, A&A, 571, A28

Planck Collaboration XXIX. 2014, A&A, 571, A29

Planck Collaboration I. 2016, A&A, 594, A1

Planck Collaboration II. 2016, A&A, 594, A2

Planck Collaboration III. 2016, A&A, 594, A3

Planck Collaboration IV. 2016, A&A, 594, A4

Planck Collaboration V. 2016, A&A, 594, A5

Planck Collaboration VI. 2016, A&A, 594, A6

Planck Collaboration VII. 2016, A&A, 594, A7

Planck Collaboration VIII. 2016, A&A, 594, A8

Planck Collaboration IX. 2016, A&A, 594, A9

Planck Collaboration X. 2016, A&A, 594, A10

Planck Collaboration XI. 2016, A&A, 594, A11

Planck Collaboration XII. 2016, A&A, 594, A12

Planck Collaboration XIII. 2016, A&A, 594, A13

Planck Collaboration XV. 2016, A&A, 594, A15

Planck Collaboration XX. 2016, A&A, 594, A20

Planck Collaboration XXII. 2016, A&A, 594, A22

Planck Collaboration XXVI. 2016, A&A, 594, A26

Planck Collaboration XXVII. 2016, A&A, 594, A27

Planck Collaboration Int. XXX. 2016, A&A, 586, A133

Plaszczynski, S., Lavabre, A., Perotto, L., & Starck, J.-L. 2012, A&A, 544, A27

Polnarev, A. G. 1985, Sov. Astron., 29, 607

Seljak, U., & Zaldarriaga, M. 1997, Phys. Rev. Lett., 78, 2054

Sherwin, B. D., & Schmittfull, M. 2015, Phys. Rev. D, 92, 043005

Simard, G., Hanson, D., & Holder, G. 2015, ApJ, 807, 166

Smith, K. M., Cooray, A., Das, S., et al. 2009a, in AIP Conf. Ser. 1141, eds. S. Dodelson, D. Baumann, A. Cooray, et al., 121

Smith, K. M., Cooray, A., Das, S., et al. 2009b, in AIP Conf. Ser. 1141, eds. S. Dodelson, D. Baumann, A. Cooray, et al., 121

Song, Y.-S., Cooray, A., Knox, L., & Zaldarriaga, M. 2003, ApJ, 590, 664

Spergel, D. N., & Zaldarriaga, M. 1997, Phys. Rev. Lett., 79, 2180

Starobinsky, A. A. 1979, Pisma v Zh. Eksp. Teor. Fiz., 30, 719

Starobinsky, A. A. 1982, Phys. Lett. B, 117, 175

Tegmark, M., Taylor, A. N., & Heavens, A. F. 1997, ApJ, 480, 22

The Polarbear Collaboration. 2014, ApJ, 794, 171

van Engelen, A., Sherwin, B. D., Sehgal, N., et al. 2015, ApJ, 808, 7

Zaldarriaga, M., & Seljak, U. 1998, Phys. Rev. D, 58, 023003

Zaldarriaga, M., & Seljak, U. 1999, Phys. Rev. D, 59, 123507

[1] APC, AstroParticule et Cosmologie, Université Paris Diderot, CNRS/IN2P3, CEA/lrfu, Observatoire de Paris, Sorbonne Paris Cité, 10 rue Alice Domon et Léonie Duquet, 75205 Paris Cedex 13, France

[2] Aalto University Metsähovi Radio Observatory and Dept of Radio Science and Engineering, PO Box 13000, 00076 Aalto, Finland

[3] African Institute for Mathematical Sciences, 6–8 Melrose Road, Muizenberg, 00040 Cape Town, South Africa

[4] Agenzia Spaziale Italiana Science Data Center, via del Politecnico snc, 00133 Roma, Italy

[5] Aix Marseille Université, CNRS, LAM (Laboratoire d'Astrophysique de Marseille) UMR 7326, 13388 Marseille, France

[6] Astrophysics Group, Cavendish Laboratory, University of Cambridge, J J Thomson Avenue, Cambridge CB3 0HE, UK

[7] Astrophysics & Cosmology Research Unit, School of Mathematics, Statistics & Computer Science, University of KwaZulu-Natal, Westville Campus, Private Bag X54001, 4000 Durban, South Africa

[8] CGEE, SCS Qd 9, Lote C, Torre C, 4° andar, Ed. Parque Cidade Corporate, CEP 70308-200 Brasília, DF, Brazil

[9] CITA, University of Toronto, 60 St. George St., Toronto, ON M5S 3H8, Canada

[10] CNRS, IRAP, 9 Av. colonel Roche, BP 44346, 31028 Toulouse Cedex 4, France

[11] CRANN, Trinity College, Dublin, Ireland

[12] California Institute of Technology, Pasadena, California, CA 911098 USA

[13] Centro de Estudios de Física del Cosmos de Aragón (CEFCA), Plaza San Juan, 1, planta 2, 44001 Teruel, Spain

[14] Computational Cosmology Center, Lawrence Berkeley National Laboratory, Berkeley, California, USA

[15] DSM/Irfu/SPP, CEA-Saclay, 91191 Gif-sur-Yvette Cedex, France

[16] DTU Space, National Space Institute, Technical University of Denmark, Elektrovej 327, 2800 Kgs. Lyngby, Denmark

[17] Département de Physique Théorique, Université de Genève, 24 Quai E. Ansermet, 1211 Genève 4, Switzerland

[18] Departamento de Astrofísica, Universidad de La Laguna (ULL), 38206 La Laguna, Tenerife, Spain

[19] Departamento de Física, Universidad de Oviedo, Avda. Calvo Sotelo s/n, 33007 Oviedo, Spain

[20] Department of Astronomy and Astrophysics, University of Toronto, 50 Saint George Street, Toronto, Ontario, Canada

[21] Department of Astrophysics/IMAPP, Radboud University Nijmegen, PO Box 9010, 6500 GL Nijmegen, The Netherlands

[22] Department of Physics & Astronomy, University of British Columbia, 6224 Agricultural Road, Vancouver, British Columbia, Canada

[23] Department of Physics and Astronomy, Dana and David Dornsife College of Letter, Arts and Sciences, University of Southern California, Los Angeles, CA 90089, USA

[24] Department of Physics and Astronomy, University College London, London WC1E 6BT, UK

[25] Department of Physics, Gustaf Hällströmin katu 2a, University of Helsinki, 00560 Helsinki, Finland

[26] Department of Physics, Princeton University, Princeton, New Jersey, NJ 08544, USA

[27] Department of Physics, University of California, One Shields Avenue, Davis, California, CA 93106, USA

[28] Department of Physics, University of California, Santa Barbara, CA 93106 California, USA

[29] Department of Physics, University of Illinois at Urbana-Champaign, 1110 West Green Street, Urbana, IL 61801 Illinois, USA

[30] Dipartimento di Fisica e Astronomia G. Galilei, Università degli Studi di Padova, via Marzolo 8, 35131 Padova, Italy

[31] Dipartimento di Fisica e Scienze della Terra, Università di Ferrara, via Saragat 1, 44122 Ferrara, Italy

[32] Dipartimento di Fisica, Università La Sapienza, P. le A. Moro 2, 00133 Roma, Italy

[33] Dipartimento di Fisica, Università degli Studi di Milano, via Celoria 16, 20133 Milano, Italy

[34] Dipartimento di Matematica, Università di Roma Tor Vergata, via della Ricerca Scientifica, 1, 00133 Roma, Italy

[35] Discovery Center, Niels Bohr Institute, Blegdamsvej 17, 1165 Copenhagen, Denmark

[36] Discovery Center, Niels Bohr Institute, Copenhagen University, Blegdamsvej 17, 1165 Copenhagen, Denmark

[37] European Space Agency, ESAC, Planck Science Office, Camino bajo del Castillo, s/n, Urbanización Villafranca del Castillo, 28691 Villanueva de la Cañada, Madrid, Spain

[38] European Space Agency, ESTEC, Keplerlaan 1, 2201 AZ Noordwijk, The Netherlands

[39] Facoltà di Ingegneria, Università degli Studi e-Campus, via Isimbardi 10, 22060 Novedrate (CO), Italy

[40] Gran Sasso Science Institute, INFN, viale F. Crispi 7, 67100 L'Aquila, Italy

[41] HGSFP and University of Heidelberg, Theoretical Physics Department, Philosophenweg 16, 69120 Heidelberg, Germany

[42] Helsinki Institute of Physics, Gustaf Hällströmin katu 2, University of Helsinki, Helsinki, Finland

[43] INAF–Osservatorio Astronomico di Padova, Vicolo dell'Osservatorio 5, 35131 Padova, Italy

[44] INAF–Osservatorio Astronomico di Roma, via di Frascati 33, 00040 Monte Porzio Catone, Italy

[45] INAF–Osservatorio Astronomico di Trieste, via G.B. Tiepolo 11, Trieste, Italy

[46] INAF/IASF Bologna, via Gobetti 101, 40126 Bologna, Italy

[47] INAF/IASF Milano, via E. Bassini 15, 20133 Milano, Italy

[48] INFN, Sezione di Bologna, via Irnerio 46, 40126 Bologna, Italy

[49] INFN, Sezione di Roma 1, Università di Roma Sapienza, Piazzale Aldo Moro 2, 00185 Roma, Italy

[50] INFN, Sezione di Roma 2, Università di Roma Tor Vergata, via della Ricerca Scientifica, 1, 00133 Roma, Italy

[51] IUCAA, Post Bag 4, Ganeshkhind, Pune University Campus, 411 007 Pune, India

[52] Imperial College London, Astrophysics group, Blackett Laboratory, Prince Consort Road, London, SW7 2AZ, UK

[53] Infrared Processing and Analysis Center, California Institute of Technology, Pasadena, CA 91125, USA

[54] Institut d'Astrophysique Spatiale, CNRS (UMR8617) Université Paris-Sud 11, Bâtiment 121, 91898 Orsay, France

[55] Institut d'Astrophysique de Paris, CNRS (UMR7095), 98bis Boulevard Arago, 75014 Paris, France

[56] Institute of Astronomy, University of Cambridge, Madingley Road, Cambridge CB3 0HA, UK

[57] Institute of Theoretical Astrophysics, University of Oslo, Blindern, 0371 Oslo, Norway

[58] Instituto de Astrofísica de Canarias, C/Vía Láctea s/n, La Laguna, 38205 Tenerife, Spain

[59] Instituto de Física de Cantabria (CSIC-Universidad de Cantabria), Avda. de los Castros s/n, 39005 Santander, Spain

[60] Istituto Nazionale di Fisica Nucleare, Sezione di Padova, via Marzolo 8, 35131 Padova, Italy

[61] Jet Propulsion Laboratory, California Institute of Technology, 4800 Oak Grove Drive, Pasadena, California, USA

[62] Jodrell Bank Centre for Astrophysics, Alan Turing Building, School of Physics and Astronomy, The University of Manchester, Oxford Road, Manchester, M13 9PL, UK

[63] Kavli Institute for Cosmological Physics, University of Chicago, Chicago, IL 60637, USA

[64] Kavli Institute for Cosmology Cambridge, Madingley Road, Cambridge, CB3 0HA, UK

[65] Kazan Federal University, 18 Kremlyovskaya St., 420008 Kazan, Russia

[66] LAL, Université Paris-Sud, CNRS/IN2P3, 91898 Orsay, France

[67] LERMA, CNRS, Observatoire de Paris, 61 Avenue de l'Observatoire, 75000 Paris, France

[68] Laboratoire AIM, IRFU/Service d'Astrophysique – CEA/DSM – CNRS – Université Paris Diderot, Bât. 709, CEA-Saclay, 91191 Gif-sur-Yvette Cedex, France

[69] Laboratoire Traitement et Communication de l'Information, CNRS (UMR 5141) and Télécom ParisTech, 46 rue Barrault 75634 Paris Cedex 13, France

[70] Laboratoire de Physique Subatomique et Cosmologie, Université Grenoble-Alpes, CNRS/IN2P3, 53 rue des Martyrs, 38026 Grenoble Cedex, France

[71] Laboratoire de Physique Théorique, Université Paris-Sud 11 & CNRS, Bâtiment 210, 91405 Orsay, France

[72] Lawrence Berkeley National Laboratory, Berkeley, California CA 94720, USA

[73] Lebedev Physical Institute of the Russian Academy of Sciences, Astro Space Centre, 84/32 Profsoyuznaya st., 117997 Moscow, GSP-7, Russia

[74] Max-Planck-Institut für Astrophysik, Karl-Schwarzschild-Str. 1, 85741 Garching, Germany

[75] National University of Ireland, Department of Experimental Physics, Maynooth, Co. Kildare, Ireland

[76] Nicolaus Copernicus Astronomical Center, Bartycka 18, 00-716 Warsaw, Poland

[77] Niels Bohr Institute, Blegdamsvej 17, 1165 Copenhagen, Denmark

[78] Niels Bohr Institute, Copenhagen University, Blegdamsvej 17, 1165 Copenhagen, Denmark

[79] Nordita (Nordic Institute for Theoretical Physics), Roslagstullsbacken 23, 106 91 Stockholm, Sweden

[80] Optical Science Laboratory, University College London, Gower Street, London, UK

[81] SISSA, Astrophysics Sector, via Bonomea 265, 34136 Trieste, Italy

[82] School of Physics and Astronomy, Cardiff University, Queens Buildings, The Parade, Cardiff, CF24 3AA, UK

[83] School of Physics and Astronomy, University of Nottingham, Nottingham NG7 2RD, UK

[84] Sorbonne Université-UPMC, UMR7095, Institut d'Astrophysique de Paris, 98bis Boulevard Arago, 75014 Paris, France

[85] Space Research Institute (IKI), Russian Academy of Sciences, Profsoyuznaya Str, 84/32, 117997 Moscow, Russia

[86] Space Sciences Laboratory, University of California, Berkeley, CA 94720 California, USA

[87] Special Astrophysical Observatory, Russian Academy of Sciences, Nizhnij Arkhyz, Zelenchukskiy region, 369167 Karachai-Cherkessian Republic, Russia

[88] Sub-Department of Astrophysics, University of Oxford, Keble Road, Oxford OX1 3RH, UK

[89] The Oskar Klein Centre for Cosmoparticle Physics, Department of Physics, Stockholm University, AlbaNova, 106 91 Stockholm, Sweden

[90] UPMC Univ Paris 06, UMR7095, 98bis Boulevard Arago, 75014 Paris, France

[91] Université de Toulouse, UPS-OMP, IRAP, 31028 Toulouse Cedex 4, France

[92] University of Granada, Departamento de Física Teórica y del Cosmos, Facultad de Ciencias, 18071 Granada, Spain

[93] University of Granada, Instituto Carlos I de Física Teórica y Computacional, 18071 Granada, Spain

[94] Warsaw University Observatory, Aleje Ujazdowskie 4, 00-478 Warszawa, Poland